Remote Sensing of Environment 133 (2013) 168–182

Contents lists available at SciVerse ScienceDirect

Remote Sensing of Environment

journal homepage: www.elsevier.com/locate/rse

Uncertainties of SeaWiFS and MODIS remote sensing reflectance: Implications from clear water measurements

Chuanmin Hu [a,*], Lian Feng [a,b], Zhongping Lee [c]

[a] University of South Florida 140 Seventh Avenue, South, St. Petersburg, FL, 33701, United States
[b] Wuhan University, State Key Laboratory of Information Engineering in Surveying, Mapping and Remote Sensing, Wuhan 430079, China
[c] University of Massachusetts at Boston, Boston, MA, 02125, United States

ARTICLE INFO

Article history:
Received 27 September 2012
Received in revised form 28 January 2013
Accepted 10 February 2013
Available online 15 March 2013

Keywords:
SeaWiFS
MODIS
GEO-CAPE
PACE
Remote sensing
Remote sensing reflectance
Uncertainty
Calibration
Validation

ABSTRACT

A fundamental parameter derived from satellite ocean color measurements is the spectral remote sensing reflectance, $R_{rs}(\lambda)$ (sr^{-1}), which is used as the input to all inversion algorithms to derive bio-optical properties (e.g., chlorophyll-a concentration or Chl in mg m^{-3}) and water's inherent optical properties (IOPs). The accuracy and uncertainties of the satellite-derived R_{rs} have only been assessed through comparisons with in situ measurements that were often limited in both space and time. Here, a novel approach was developed and used to estimate R_{rs} uncertainties from SeaWiFS and MODIS/Aqua (MODISA) measurements over clear waters. The study focused on two oligotrophic ocean gyres in the North Atlantic and South Pacific, and used a recently developed new Chl algorithm to provide a constraint to determine the highest-quality R_{rs} data with minimal errors. These data were used as surrogates of "ground truth" or references (termed as $R_{rs,true}$) to estimate the R_{rs} error in each data point, with uncertainty estimates (in both relative and absolute forms) generated from statistical analyses. The study led to several findings: One, both SeaWiFS and MODISA have met their mission goals of achieving R_{rs} uncertainties and absolute accuracy (assuming that the $R_{rs,true}$ values can represent the truth) to within 5% for blue bands and blue waters. As a comparison, nearly all previous in situ-based validation efforts reported mean (or median) percentage differences exceeding 10% between in situ and satellite R_{rs} in the blue bands. Two, for the green bands, R_{rs} uncertainties are significantly higher, often in the range of 10–15% for oligotrophic waters. Three, SeaWiFS R_{rs} uncertainties are generally higher than those of MODISA, possibly due to its lower signal-to-noise ratio (SNR). Four, all R_{rs} errors are spectrally related in a monotonous way from the blue to the red wavelengths, suggesting that these errors are resulted primarily from the imperfect atmospheric correction algorithms as opposed to sensor noise or vicarious calibration. Such empirical relationships are shown to be useful in reducing the R_{rs} uncertainties for the North Atlantic Gyre and may also be useful for most of the ocean waters. Finally, the tabulated results provide lower bounds of $R_{rs}(\lambda)$ uncertainties for more productive waters. The findings may serve as references for future ocean color missions, and they have also significant implications for uncertainty estimates of other ocean color data products.

1. Introduction

Ocean color missions often call for accuracy goals of 5% and 35% for the retrieved surface remote sensing reflectance (R_{rs}, sr^{-1}) in the blue bands and chlorophyll-a concentrations (Chl, mg m^{-3}) in the surface ocean, respectively, for clear-ocean waters (Hooker et al., 1992). Whether or not such goals are met have been assessed through extensive validation, where a comprehensive in situ data set with measurements covering a wide range of oceanographic conditions is essential (Werdell and Bailey, 2005). Such a requirement has been fully recognized since the early 1990s (Hooker and McClain, 2000; Hooker et al., 1992). As a result, a repository of in situ bio-optical data, namely the SeaWiFS Bio-optical Archive and Storage System (SeaBASS) (Hooker et al., 1994; Werdell et al., 2003), has been populated with both funded and voluntary data contributions from investigators worldwide (Fargion et al., 2004).

Using this global data archive, Bailey and Werdell (2006) showed that the median absolute percentage difference (MPD) between SeaWiFS and in situ normalized water-leaving radiance (L_{wn}, equivalent to R_{rs}) for the global deep-waters (>1000 m bottom depth) ranged between 10.78% and 16.64% for the 5 bands from 412 to 555 nm (Table 2 of Bailey and Werdell, 2006). This is 2–3 times of the 5% mission goal. Even after subtracting the potential 3–5% uncertainties in the in situ data (Hooker and Maritorena, 2000), the remaining uncertainties still exceeded the mission goal slightly, not to mention whether the in situ uncertainties can be separated from a direct subtraction. If data from shallower oceans were included, the uncertainties were even higher.

Validation efforts using regional cruise surveys or buoys showed similar results. Antoine et al. (2008) used water-leaving reflectance

* Corresponding author.
E-mail address: huc@usf.edu (C. Hu).

0034-4257/$ – see front matter © 2013 Elsevier Inc. All rights reserved.
http://dx.doi.org/10.1016/j.rse.2013.02.012

($\rho_w = \pi R_{rs}$) from underwater measurements at an offshore site (the BOUSSOLE buoy) in the Mediterranean Sea between 2003 and 2006 to validate ρ_w derived from MODISA, SeaWiFS, and MERIS measurements. They reported that the average relative (signed) percent differences (RPD) between satellite and in situ ρ_w at 443 and 490 nm were within 5% for both SeaWiFS and MODISA. However, when the average absolute (unsigned) percentage difference (|RPD|) is used as a measure of uncertainty, as suggested by the authors, none of the spectral bands of the three sensors met the 5% mission goal. Even for the 443 and 490 bands of SeaWiFS and MODISA where the least uncertainties were found, |RPD| still exceeded 11%. These uncertainty estimates agree well with those determined from coastal sites in some European waters including the Adriatic Sea (Mélin et al., 2007; Zibordi et al., 2006, 2009). Even after an overall 6% uncertainty from the in situ measurements is subtracted (the 6% uncertainty was estimated from various error sources from in situ measurements: 3% for radiometric calibration, 2% for calibration decay over time, 3% for surface extrapolation, 3% for self-shading correction, 2% for bidirectional effects, see Antoine et al. (2008) for more details), the remaining uncertainties still exceeded the 5% mission goal. On the other hand, uncertainties in the in situ R_{rs} from either below-water or above-water measurements can be significantly higher than 6% (Harmel et al., 2012; Toole et al., 2000).

Slightly better results were obtained from a shallow shelf in the eastern Gulf of Mexico. Using repeated bio-optical measurements during two major field programs spanning over a decade on the West Florida Shelf, Cannizzaro et al. (in press) evaluated the uncertainties of the SeaWiFS L_{wn} data (412–555 nm), and found 7–9% uncertainties when aerosol optical thicknesses at 865 nm ($\tau_a 865$) were less than 0.14, accounting for >90% of the time for this region over the SeaWiFS mission. Uncertainties increased to 10–14% when all data were considered. Note that these uncertainties estimates also had uncertainties of in situ data embedded.

There is one possible limitation in the above in situ-based validation and uncertainty assessment efforts: data coverage. Regardless of the amount of effort, in situ data are always limited in both time and space, and the validation statistics are valid only for the measurement conditions where and when the in situ data are collected. For example, only ~40% of the radiometric data in the SeaBASS archive are from deep-water (>1000 m bottom depth) measurements, and <5% of these data are from oligotrophic waters (Chl<0.1 mg m^{-3}) (Bailey and Werdell, 2006). Likewise, only ~5% of the Chl data in the archive are from oligotrophic waters. On the other hand, ~77% of the global ocean has Chl<0.25 mg m^{-3} and 38% of the global ocean has Chl<0.1 mg m^{-3}. As a result, potential biases may be introduced in the global ocean statistics even if the in situ validation (from un-balanced global ocean sampling) shows little bias, because each individual in situ point in the validation may represent a weight different from its realistic weight in the global data distributions (Moore et al., 2009). Adding on top of this limitation is the difficulty in separating the uncertainties in the in situ data, which can be >12% (Toole et al., 2000), from uncertainties in the satellite data. In coastal waters, the difference between in situ and satellite R_{rs} may also result from their different spatial coverage. In short, what the satellite—in situ comparisons provide are statistics of differences between satellite and in situ products, and not necessarily uncertainties of the satellite products.

Figs. 1 and 2 show two examples of apparent errors in the satellite R_{rs} products that might not be captured by the less frequent in situ measurements. The errors are obvious because optical properties of these clear waters are well known. Fig. 1 shows two images of $R_{rs}(555)$ and $R_{rs}(547)$ from SeaWiFS and MODISA measurements, respectively, near the center of the North Atlantic Gyre. Instead of showing relatively homogeneous values in this ocean gyre, as explained by both radiative transfer theory and field measurements (Gordon and Clark, 1981; Morel and Maritorena, 2001; Morel et al., 2007), the images show patchiness and significant spatial variability, leading to R_{rs} values far beyond their theoretical limits. Likewise, the time series of the SeaWiFS $R_{rs}(555)$ data over an oligotrophic site in the North Atlantic Gyre shows not only pixelization noise, as measured by the standard deviation of the 3×3 pixels, but also temporal inconsistency (i.e., values from adjacent days "jump" from each other) (Fig. 2a). Correspondingly, Chl data derived from the $R_{rs}(443)/R_{rs}(555)$ ratio and a band-ratio algorithm (O'Reilly et al., 2010, hereafter referred to as "Chl_{OCX}") show similar noises and errors (Fig. 2b).

Note that all non-zero pixels shown in Figs. 1 and 2 have passed through the quality control flags (see Data and methods section) and are thus regarded as valid and used in the global data composites. Some of the errors associated with satellite data (e.g., random sensor noise) may be canceled in the data binning, but others (e.g., errors in atmospheric correction) may remain and they represent a significant error source that cannot be removed in the global composites, thus leading to potential biases in global or even regional studies. On the other hand, these noises and errors may not be captured by the less frequent in situ measurements. It is therefore critical to understand the data product uncertainties using realistic satellite measurements at synoptic spatial and temporal scales covering all possible scenarios.

Hence, an image-based approach could fulfill the needs for unbiased sampling because satellite images could cover all measurement conditions. In practice, however, the fundamental problem of this approach is the difficulty in finding the "true" R_{rs} (hereafter referred to as $R_{rs,true}$) for a given location and time, from which R_{rs} errors of individual pixels and R_{rs} uncertainties of all pixels can be referenced. Without knowing the $R_{rs,true}$ values, statistics of all R_{rs} values derived from satellite measurements can only be used to calculate the means and anomalies, with the anomalies not interpreted as R_{rs} uncertainties but used to represent realistic ocean variations due to changes of colored dissolved organic matter (CDOM) and/or particle backscattering (b_{bp}) relative to Chl (Brown et al., 2008).

The recent development of a novel Chl algorithm for oligotrophic oceans (Hu et al., 2012b) may solve this problem through finding $R_{rs,true}$ for each clear-water site. The color index (CI) algorithm uses a 3-band subtraction method (443, 555, and 670 nm) instead of a band-ratio method (443/555 ratio) to derive an empirical Chl, thus is nearly immune to all additive errors that result from atmospheric correction (Gordon, 1997; Gordon and Wang, 1994a), whitecap correction (Frouin et al., 1996; Gordon and Wang, 1994b), and sun glint correction (Wang and Bailey, 2001). The method has been proven superior to the traditional band-ratio methods in all measures (simulations, in situ validation, data statistics) for waters with Chl ≤ 0.25 mg m^{-3}. For example, a bias of 0.0015 sr^{-1} is equivalent to 100% relative error in $R_{rs}(555)$ for blue waters, but it will only lead to a 2% relative error in the derived Chl_{CI}. Fig. 2c shows an example of the improved Chl_{CI} time-series as compared with the error-prone Chl_{OCX} time series in Fig. 2b. Not only was pixelization noise (as measured by the 3×3 standard error bars) removed nearly completely, the unrealistic day-to-day "jumps" were also minimized significantly. Note that in the notation Chl_{CI} is termed as Chl_{OCI} because the latter is a merged algorithm between Chl_{CI} (for low Chls) and Chl_{OCX} (for higher Chls). For the oligotrophic waters with Chl ≤ 0.25 mg m^{-3}, Chl_{OCI} is identical to Chl_{CI}.

Thus, the difference between the error-immune Chl_{OCI} and error-prone Chl_{OCX} may be used as a constraint to determine $R_{rs,true}$. The logic is that if the input R_{rs} data are error free, Chl_{OCI} and Chl_{OCX} are nearly the same (Hu et al., 2012b). Vice versa, if Chl_{OCI} and Chl_{OCX} differ significantly, the input R_{rs} data must contain errors. Thus, the constraint can be used to select pixels that meet or fail the criterion of $Chl_{OCX} \approx Chl_{OCI}$ for blue waters, from which $R_{rs,true}$ and R_{rs} errors can be determined. Note that the term "true" does not mean the theoretical true reflectance, but serves as a reference determined from the $Chl_{OCX} \approx Chl_{OCI}$ constraint. Fig. 2c and the many other examples presented in Hu et al. (2012b) suggest that this idea can be

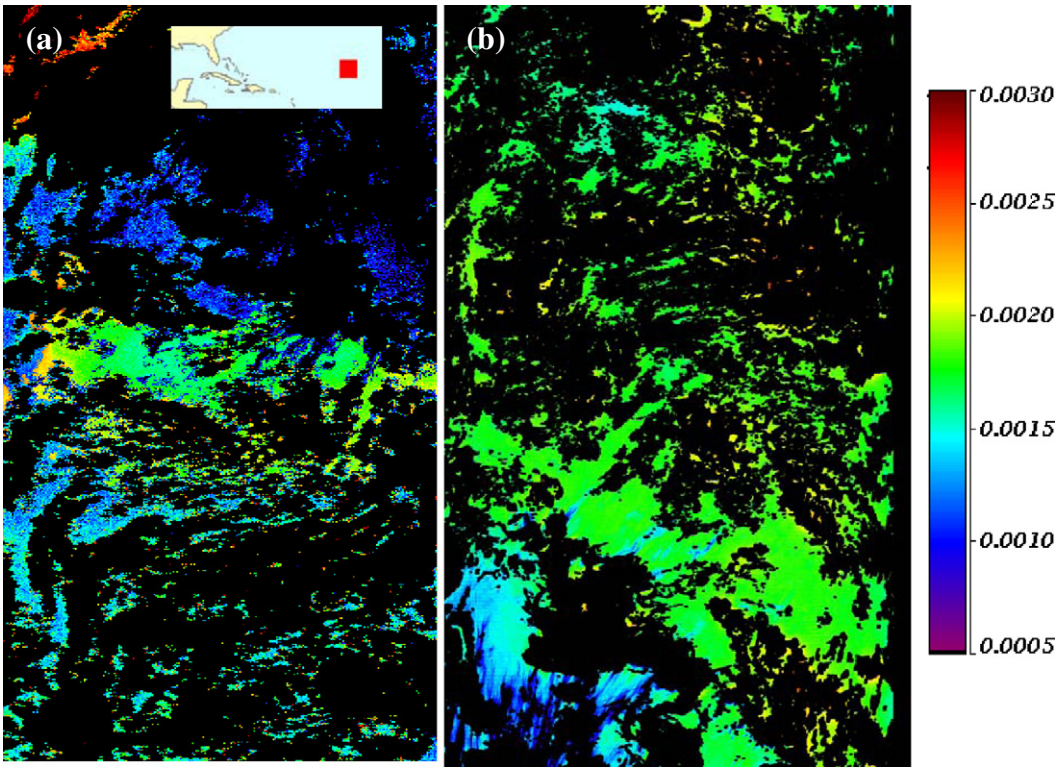

Fig 1. SeaWiFS $R_{rs}(555)$ (a) and MODISA $R_{rs}(547)$ (b) in the North Atlantic Gyre on 27 December 2006. Both images are about 1500 km×1500 km centered at 23°N 47°W (inset figure). Black represents clouds, algorithm failure, or pixels associated with any of the quality control flags. All other colors are treated as valid data and used in the global composites.

implemented to quantify R_{rs} uncertainties for blue waters, which may have several advantages over traditional field-based validation methods (see Discussion section).

Based on the above proof-of-concept, we performed extensive data analyses of selected SeaWiFS and MODISA data, with the following objectives:

1. Quantify SeaWiFS and MODISA R_{rs} uncertainties in both absolute and relative units over blue waters. These uncertainty estimates may serve as the lower bounds for R_{rs} uncertainties over coastal oceans, as the latter are more prone to atmospheric correction errors and other perturbations;
2. Revisit the ocean color mission goal of achieving <5% R_{rs} errors in absolute accuracy in the blue bands for clear waters. After all, have SeaWiFS and MODISA met their mission goals, after numerous reports of their >10% differences from in situ validations?
3. Provide baseline and reference data for future works in quantifying uncertainties in other ocean color data products (e.g., inherent optical properties or IOPs) and in designing other ocean color missions.

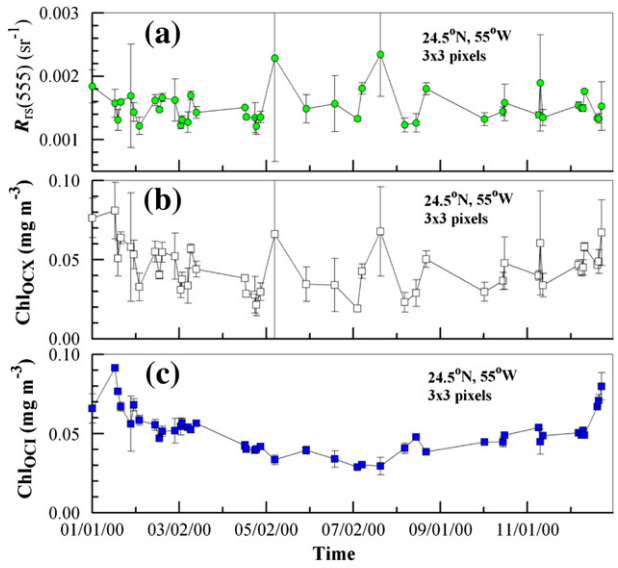

Fig. 2. SeaWiFS data products at a location in the North Atlantic Gyre. (a) $R_{rs}(555)$; (b) Chl_{OCX} from a band-ratio algorithm (O'Reilly et al., 2010); (c) Chl_{OCI} from a band-subtraction algorithm (Hu et al., 2012b). The standard deviation bar represents the 3×3 pixel variability centered at the location.

The paper starts with description of the satellite data and methods used to derive the R_{rs} references ($R_{rs,true}$, used as surrogates of "ground truth") and R_{rs} uncertainties against these references for both SeaWiFS and MODISA measurements. Then, results of the derived R_{rs} references and R_{rs} uncertainties are presented in detail in both tabular and graphic forms, followed by discussions on how to interpret these data, the sources of R_{rs} uncertainties, and implications for measurements over more turbid waters and for future satellite ocean color missions.

2. Data and methods

To meet the requirements of spatially homogeneous and temporarily stable ocean targets for R_{rs} uncertainty assessment, two areas were selected in this study: a 20×20° area near the North Atlantic Gyre and a 20×20° area near the South Pacific Gyre (Fig. 3). These two areas have the clearest ocean waters on Earth (Morel et al., 2007), and analysis of SeaWiFS data using the criteria of reflectance constraints showed that both areas belonged to the category of Case-1 waters (Lee and Hu, 2006). The two areas represent two contrasting atmospheric environment: one in the northern hemisphere where most of the world's land and populations reside, and the other in the southern hemisphere with less land and populations.

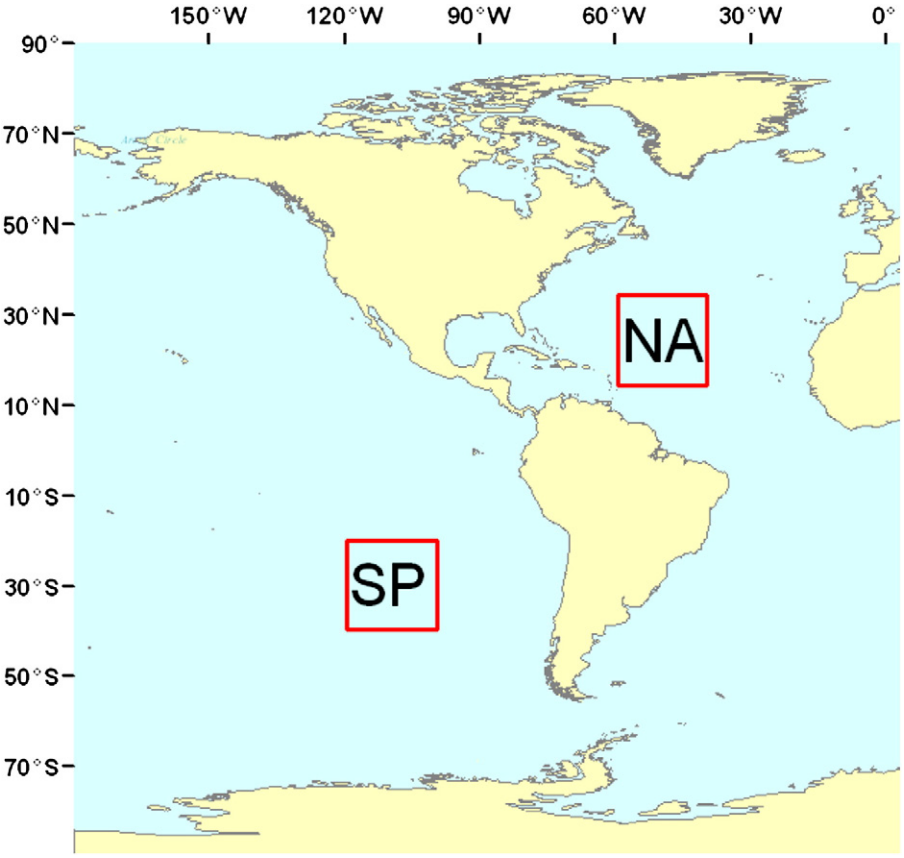

Fig. 3. SeaWiFS and MODISA data used in this study are from the South Pacific (SP, 120°–100°W, 20°–40°S) and North Atlantic (NA, 60°–40°W, 15°–35°N). Annual mean aerosol optical thickness at 865 nm (τ865) derived from SeaWiFS for 2006 is 0.071 ± 0.016 and 0.058 ± 0.014 for NA and SP, respectively.

These two areas experience different aerosol influence (Wang, M., et al. (2005)), thus providing two contrasting environments to evaluate product uncertainties. Annual mean aerosol optical thickness at 865 nm (τ865) derived from SeaWiFS for 2006 is 0.071 ± 0.016 and 0.058 ± 0.014 for the North Atlantic Gyre and South Pacific Gyre, respectively.

MODISA local-area-coverage (LAC) and SeaWiFS global-area-coverage (GAC) data were obtained from the NASA Goddard Space Flight Center (GSFC) through the Ocean Biological Processing Group (OBPG). Ideally, SeaWiFS LAC data should be used, but these data were not recorded onboard, and no ground station was available to cover these remote regions. The Level-2 data products, obtained from NASA OBPG, included the spectral R_{rs} for every visible band, Chl_{OCX}, aerosol optical depth (τ, 869 nm for MODISA and 865 nm for SeaWiFS) and angstrom exponent (α), and quality control flags (a 32-bit value for each image pixel, namely "l2_flags"). These products have been derived using the most recent updates in software (SeaDAS version 6.3) and in calibration and algorithm development (e.g., Ahmad et al., 2010; Franz et al., 2007; Frouin et al., 1996; Gordon, 1997; Gordon and Wang, 1994a,b; Stumpf and Werdell, 2010; Wang and Shi, 2007; Werdell and Bailey, 2005), and they represent the current state-of-the-art science-quality data products. For MODISA, 619 data files for the NA and 1611 data files for the SP were available for 2006. For SeaWiFS, 605 data files for the NA and 651 data files for the SP were available for 2006.

For each Level-2 data file, spectral R_{rs} data were extracted and used to calculate Chl_{OCI} following the methods of Hu et al. (2012b). The results were stored in a separate Level-2 data file. Then, all pixels were screened using the l2-flags bit operations, and the pixels associated with any of the following quality-control flags were discarded: ATMFAIL (1), LAND (2), HIGLINT(4), HILT (5), HISATZEN (6), STRAYLIGHT (9), CLDICE (10), COCCOLITH (11), HISOLZEN (13), LOWLW (15), CHLFAIL (16), NAVWARN (17), MAXAERITER (20), CHLWARN (22), ATMWARN (23), NAVFAIL (26), and FILTER (27). The numbers in the parentheses represent the bit position of the 32-bit flag value. This data screening procedure followed the same quality control methods for global data binning (composites). In other words all pixels that passed through the screening are valid pixels for the NASA standard Level-3 global products, and our uncertainty assessment was focused on these valid (i.e., non-flagged) pixels only.

Before implementing the computer codes for statistical analyses of this large volume of data, a test was performed to verify whether the constraint of $Chl_{OCX} \approx Chl_{OCI}$ could be used to derive $R_{rs,true}$. The test used several SeaWiFS and MODISA images of the NA in April 2005 to plot R_{rs} against Chl_{OCI} for all valid pixels, with results shown in Fig. 4. For each Chl_{OCI}, significant R_{rs} variability was found in all spectral bands. However, for the pixels meeting the $Chl_{OCX} \approx Chl_{OCI}$ constraint (numerically, it is $|(Chl_{OCx} - Chl_{OCI})/Chl_{OCI}| \leq 5\%$), the R_{rs} variability was significantly reduced, leading to the tight lines (green points in Fig. 4) for the entire Chl_{OCI} range. This statistical result agrees well with the proof-of-concept graph in Fig. 2, and suggests that 1) nearly all R_{rs} data spread for a given Chl_{OCI} from a specific oceanographic region are due to errors, and 2) the R_{rs} data meeting the constraint criterion (green points in Fig. 4) can be used as the reference or "truth" (i.e., $R_{rs,true}$) to estimate the R_{rs} uncertainties from all valid pixels for the oceanographic region.

Thus, two steps were used for the R_{rs} uncertainty assessment.

First, for each study area (NA and SP), $R_{rs,true}$ for each of the SeaWiFS and MODISA spectral bands was determined at several pre-defined Chl_{OCI} levels, ranging between 0.03 and 0.2 mg m^{-3}. For each Chl_{OCI} level (± 2% in order to find sufficient number of pixels for statistical analyses), the pixels meeting the $Chl_{OCX} \approx Chl_{OCI}$

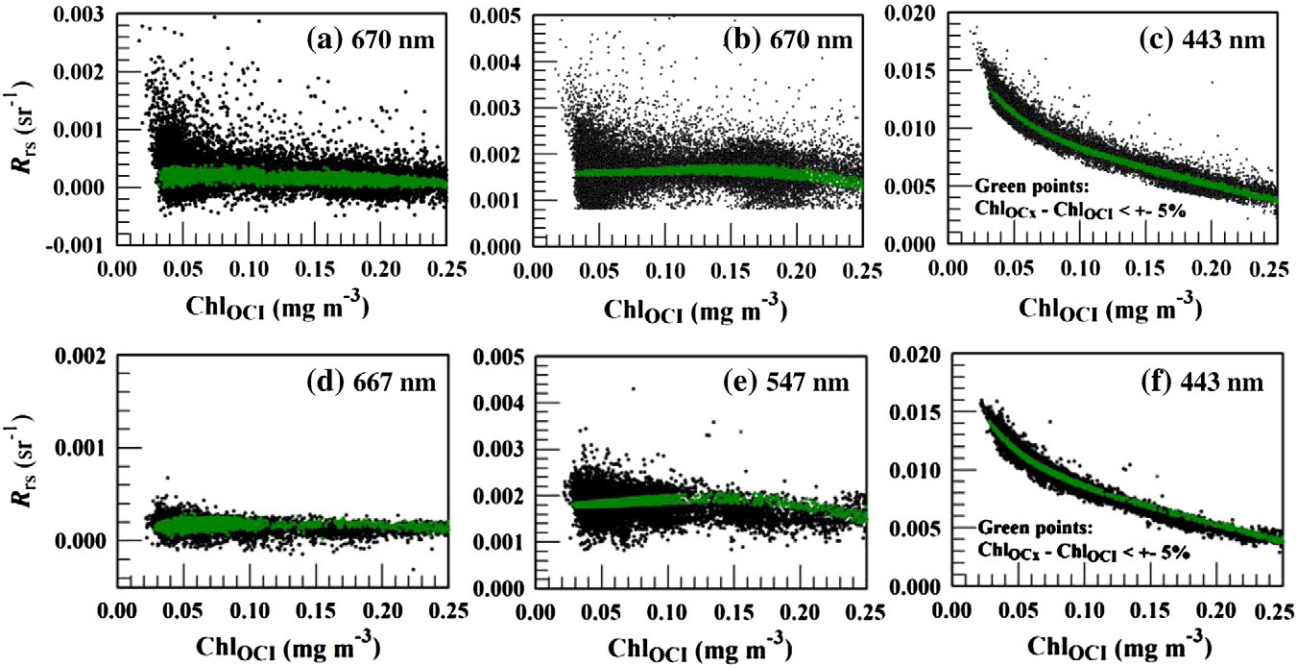

Fig. 4. SeaWiFS R_{rs} (a–c) and MODIS/Aqua R_{rs} (d–f) plotted against Chl_{OCI} for the North Atlantic Gyre from several images in April 2005 for all non-flagged data (i.e., valid data used in the global composites). The green points represent those meeting the constraint of <5% relative difference between Chl_{OCx} and Chl_{OCI}. This constraint was used in this study as a criterion to find "good" pixels (green) with minimal or no R_{rs} errors, leading to the estimation of $R_{rs,true}$ for each Chl_{OCI}. The rest are "bad" pixels even if they are regarded as valid in the global composites. For SeaWiFS, 15.4% and 84.6% are "good" and "bad" pixels, respectively. For MODIS/Aqua, 31.8% and 68.2% are "good" and "bad" pixels, respectively. Note the difference in the y-axis scales.

constraint were queried to calculate the mean and standard deviation of their R_{rs} values, with the mean representing $R_{rs,true}$ (Table 1 and Fig. 5). As mentioned before, such determined $R_{rs,true}$ values may not be the theoretical "true" R_{rs} but they represent where Chl_{OCX} and Chl_{OCI} converge, therefore serving as references to determine R_{rs} departures (errors) from these references. In practice, $Chl_{OCX} \approx Chl_{OCI}$ was defined as $|(Chl_{OCx} - Chl_{OCI})/Chl_{OCI}| \leq 5\%$, and the derived $R_{rs,true}$ values were insensitive to the 5% threshold (e.g., changes in the $R_{rs,true}$ values were <1% if a 10% threshold was used). Second, $R_{rs,true}$ determined above was used as a reference to gauge $R_{rs,}$ errors of all pixels, with statistics

Table 1
SeaWiFS and MODISA R_{rs} from North Atlantic (NA) and South Pacific (SP) determined using the constraint of <5% difference between Chl_{OCX} and Chl_{OCI}. All SeaWiFS and MODISA data during 2006 covering the study region were used in the calculations, with 605 (NA) and 651 (SP) images for SeaWiFS and 619 (NA) and 1611 (SP) images for MODISA. For the South Pacific, there are not enough valid points to draw statistics for Chl = 0.2 mg m^{-3}. Results obtained from other years are nearly identical (<1% difference). These values are used as the reference or "truth" ($R_{rs,true}$) in this study to determine the R_{rs} errors and uncertainties from the satellite measurements. Note that to enable sufficient number of pixels to be found for statistical analysis, each pre-defined Chl level was allowed to cover a ±2% interval, and a sensitivity test showed that the tabulated results were insensitive to changes in this interval. The data are presented in graphical forms in Fig. 5.

Chl (mg m^{-3})		0.03	0.05	0.1	0.15	0.2
SeaWiFS_NA	412 ($\times 10^{-2}$ sr^{-1})	1.724 ± 0.024	1.409 ± 0.046	0.945 ± 0.04	0.702 ± 0.034	0.538 ± 0.037
	443 ($\times 10^{-2}$ sr^{-1})	1.354 ± 0.007	1.128 ± 0.008	0.822 ± 0.012	0.648 ± 0.015	0.498 ± 0.020
	490 ($\times 10^{-3}$ sr^{-1})	7.548 ± 0.091	6.890 ± 0.130	5.861 ± 0.189	5.229 ± 0.241	4.226 ± 0.277
	510 ($\times 10^{-3}$ sr^{-1})	3.779 ± 0.101	3.640 ± 0.093	3.424 ± 0.133	3.308 ± 0.169	2.887 ± 0.191
	555 ($\times 10^{-3}$ sr^{-1})	1.580 ± 0.019	1.593 ± 0.025	1.619 ± 0.043	1.638 ± 0.060	1.523 ± 0.081
	670 ($\times 10^{-4}$ sr^{-1})	2.013 ± 0.343	2.122 ± 0.368	2.239 ± 0.565	1.835 ± 0.607	1.748 ± 0.567
SeaWiFS_SP	412 ($\times 10^{-2}$ sr^{-1})	1.829 ± 0.052	1.478 ± 0.052	1.012 ± 0.035	0.804 ± 0.036	N/A
	443 ($\times 10^{-2}$ sr^{-1})	1.351 ± 0.008	1.129 ± 0.009	0.824 ± 0.011	0.655 ± 0.015	N/A
	490 ($\times 10^{-3}$ sr^{-1})	7.381 ± 0.122	6.947 ± 0.255	5.951 ± 0.213	5.310 ± 0.204	N/A
	510 ($\times 10^{-3}$ sr^{-1})	3.719 ± 0.093	3.685 ± 0.150	3.551 ± 0.125	3.442 ± 0.161	N/A
	555 ($\times 10^{-3}$ sr^{-1})	1.574 ± 0.019	1.592 ± 0.026	1.623 ± 0.041	1.659 ± 0.061	N/A
	670 ($\times 10^{-4}$ sr^{-1})	2.251 ± 0.399	2.066 ± 0.464	2.168 ± 0.491	1.668 ± 0.504	N/A
MODIS_NA	412 ($\times 10^{-2}$ sr^{-1})	1.734 ± 0.027	1.436 ± 0.049	0.991 ± 0.047	0.731 ± 0.035	0.557 ± 0.035
	443 ($\times 10^{-2}$ sr^{-1})	1.377 ± 0.007	1.153 ± 0.008	0.852 ± 0.011	0.679 ± 0.017	0.524 ± 0.019
	488 ($\times 10^{-3}$ sr^{-1})	7.992 ± 0.084	7.266 ± 0.100	6.213 ± 0.175	5.572 ± 0.258	4.525 ± 0.260
	531 ($\times 10^{-3}$ sr^{-1})	2.470 ± 0.045	2.448 ± 0.050	2.483 ± 0.078	2.513 ± 0.112	2.294 ± 0.121
	547 ($\times 10^{-3}$ sr^{-1})	1.802 ± 0.022	1.825 ± 0.030	1.887 ± 0.050	1.935 ± 0.080	1.796 ± 0.092
	667 ($\times 10^{-4}$ sr^{-1})	1.576 ± 0.201	1.727 ± 0.226	1.985 ± 0.326	1.921 ± 0.368	1.994 ± 0.411
	678 ($\times 10^{-4}$ sr^{-1})	1.506 ± 0.225	1.676 ± 0.270	1.943 ± 0.378	1.910 ± 0.406	2.194 ± 0.501
MODIS_SP	412 ($\times 10^{-2}$ sr^{-1})	1.874 ± 0.055	1.535 ± 0.046	1.07 ± 0.043	0.823 ± 0.052	N/A
	443 ($\times 10^{-2}$ sr^{-1})	1.374 ± 0.007	1.150 ± 0.008	0.855 ± 0.011	0.680 ± 0.019	N/A
	488 ($\times 10^{-3}$ sr^{-1})	7.761 ± 0.158	7.198 ± 0.178	6.278 ± 0.204	5.549 ± 0.254	N/A
	531 ($\times 10^{-3}$ sr^{-1})	2.429 ± 0.055	2.445 ± 0.060	2.524 ± 0.077	2.509 ± 0.125	N/A
	547 ($\times 10^{-3}$ sr^{-1})	1.791 ± 0.023	1.819 ± 0.031	1.904 ± 0.050	1.938 ± 0.080	N/A
	667 ($\times 10^{-4}$ sr^{-1})	1.841 ± 0.272	1.835 ± 0.295	1.919 ± 0.328	2.033 ± 0.603	N/A
	678 ($\times 10^{-4}$ sr^{-1})	1.771 ± 0.317	1.792 ± 0.318	2.004 ± 0.380	2.124 ± 0.597	N/A

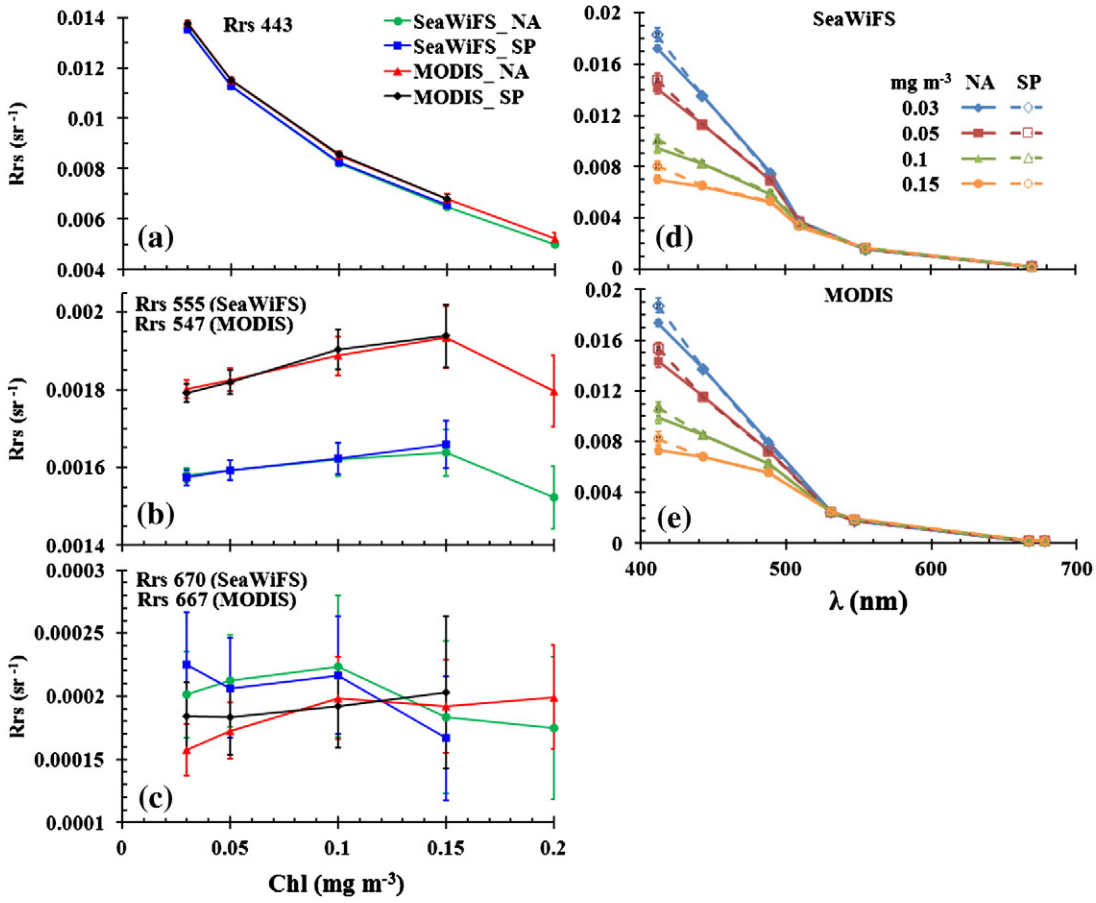

Fig. 5. $R_{rs,true}$ determined from SeaWiFS and MODISA measurements in the North Atlantic (NA) and South Pacific (SP) using a Chl constraint. These data are used as error-free R_{rs} in this study to determine R_{rs} uncertainties of all non-flagged (i.e., valid) pixels. (a)–(c): $R_{rs,true}$ as a function of Chl_{OCI} for the Red–Green–Blue bands; (d)–(e): Spectral $R_{rs,true}$ for each pre-defined Chl_{OCI} level. All data are listed in Table 1.

generated to estimate uncertainties. For each valid pixel at the pre-defined Chl_{OCI} level, the relative difference between the current R_{rs} and $R_{rs,true}$ was calculated as

$$\delta = \left(R_{rs} - R_{rs,true}\right)/R_{rs,true} \qquad (\times 100\%). \tag{1}$$

The standard deviation of δ for all valid pixels (e.g., all black and green pixels in Fig. 4), σ, was calculated and used to represent the R_{rs} uncertainty for that Chl_{OCI} level. Another measure to represent absolute accuracy, used by several other researchers (e.g., Antoine et al., 2008; Bailey and Werdell, 2006; Zibordi et al., 2006, 2009), was the mean (or median) value of |δ| for all pixels:

$$\gamma = (1/N)\sum|\delta_i|, \tag{2}$$

where N is the number of pixels. This measure of accuracy, named as mean percentage difference (MPD), was also calculated for each Chl_{OCI} level.

Finally, R_{rs} uncertainty estimates in absolute units (i.e., sr^{-1}) are desired for ocean color mission planning. For these estimates, the R_{rs} error for each pixel was calculated as

$$\Delta R_{rs} = R_{rs} - R_{rs,true}. \tag{3}$$

The standard deviation of ΔR_{rs} from all qualifying pixels was calculated as Ω, and the mean of $|\Delta R_{rs}|$ from all pixels was calculated as:

$$\Gamma = (1/N)\sum|\Delta R_{rs}|. \tag{4}$$

Here Ω and Γ correspond to relative uncertainty (σ) and MPD (γ) from Eqs. (1) and (2) above, but are expressed in reflectance units.

In these calculations, we determined to remove the impact of pixelization noises (Hu et al., 2001) on the uncertainty estimates, because these random noises, originated from either instrument digitization round-off or inherent instrument noise, are greatly reduced in the global data composites during the data binning. These global data composites instead of the Level-2 R_{rs} data are those used the most for ocean studies. These noises in our calculations were minimized through a 3×3 median filter, and the filtered R_{rs} data were used in Eqs. (1)–(4) to calculate the R_{rs} uncertainties and MPDs. A sensitivity test was also performed to compare the results with and without the median filter (Fig. 6).

To study the potential impact of various observing conditions (aerosol optical depth τ and angstrom exponent α) on the R_{rs} uncertainty estimates, all pixels were partitioned to various groups using several τ and α values, with R_{rs} uncertainties estimated for each partition.

3. Results

3.1. $R_{rs,true}$ values for clear waters

Table 1 lists the $R_{rs,true}$ values corresponding to each of the pre-defined Chl values, where the data are plotted in Fig. 5. These results agree well with those predicted by radiative transfer theory and measured in the field for clear waters (Gordon and Clark, 1981; Morel and Maritorena, 2001; Morel et al., 2007).

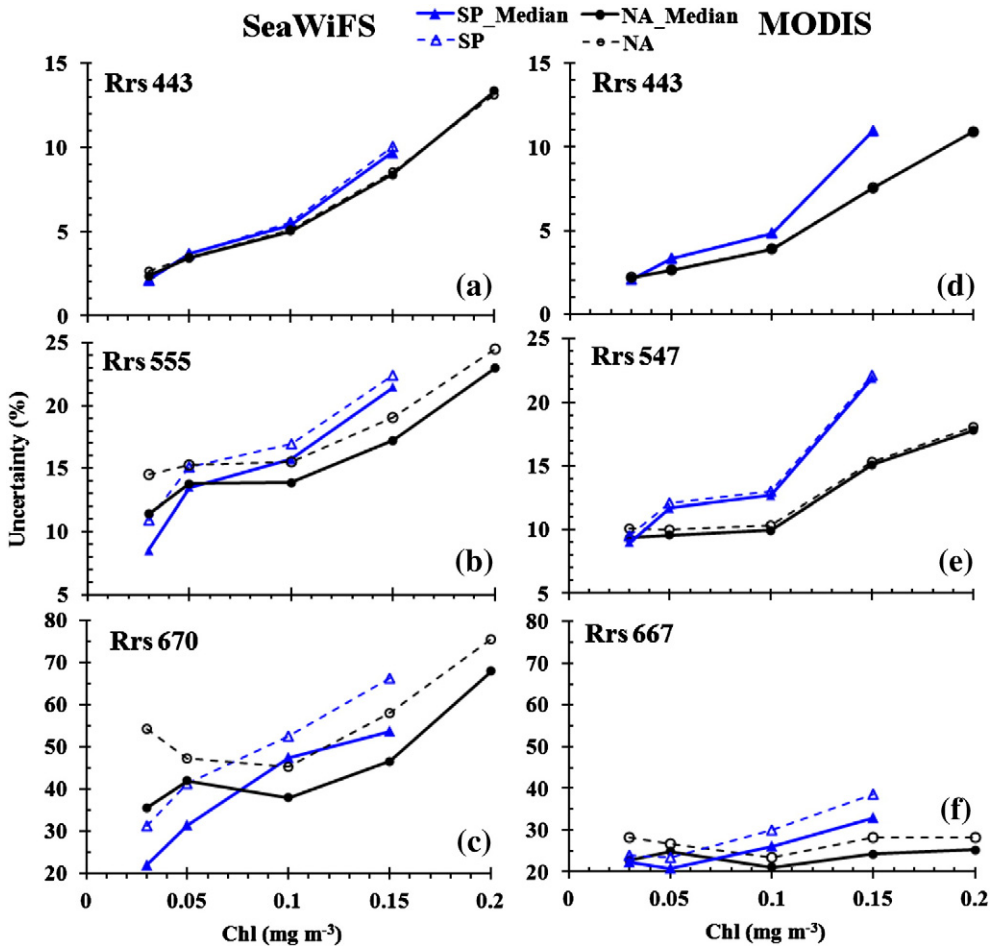

Fig. 6. Relative uncertainties (in percentage, σ from Eq. 1) of SeaWiFS and MODISA R_{rs} data for the North Atlantic (NA, black) and South Pacific (SP, blue). The x-axis is Chl_{OCI}. About 68% of the non-flagged (i.e., valid) pixels have R_{rs} errors (gauged against the corresponding $R_{rs,true}$) less than the uncertainties. The solid lines represent uncertainties with 3×3 pixelization (specking) noise removed with a median filter, and they are tabulated in Table 2. The dashed lines represent the raw R_{rs} data without filtering the noise. The noise removal only affects SeaWiFS, with minimal impact on MODISA.

For each sensor, either SeaWiFS or MODISA, excellent agreement in $R_{rs}(\lambda)$ was found between NA and SP for all but the 412-nm bands. This result further supports the approach of using the $Chl_{OCX} \approx Chl_{OCI}$ constraint to determine $R_{rs,true}$. The standard deviations around the $R_{rs,true}$ values for the blue-green bands (except 412 nm) are extremely small (<2–3%) for Chl ≤ 0.1 mg m^{-3}, suggesting very stable $R_{rs,true}$ values under all conditions. The relatively large standard deviations for the red bands (10–30%) are due to the extremely small $R_{rs,true}$ values in the red bands.

For each region (NA or SP), there is a slight relative difference (~<2%) for $R_{rs,true}(443)$ between MODISA and SeaWiFS (Fig. 5a). While the reason is not well understood, the small difference will not affect the R_{rs} uncertainty estimates as these are the measures of the data spread. The relative difference is larger between $R_{rs,true}(667)$ of MODIS and $R_{rs,true}(670)$ of SeaWiFS (Fig. 5c) because of the slight difference in the wavelengths and the small $R_{rs,true}$ values (note that the standard deviations overwhelm these cross-sensor differences). The highest relative difference was found between $R_{rs,true}(547)$ of MODIS and $R_{rs,true}(555)$ of SeaWiFS (Fig. 5b) because of the wavelength difference. For each sensor and pre-defined Chl_{OCI} level, there is also a noticeable difference in $R_{rs,true}(412)$ between NA and SP (dashed versus solid lines in Fig. 5d–e), suggesting varying proportions of CDOM absorption in the two contrasting ocean gyres (Siegel et al., 2002). Nevertheless, the relative variability around each $R_{rs,true}$ value, as measured by the standard deviations in Table 1 and Fig. 5, is much smaller than the R_{rs} data spread in Fig. 4. Thus, $R_{rs,true}$ can be used as stable references to gauge the degree of the R_{rs} spread (i.e., R_{rs} uncertainties).

3.2. R_{rs} uncertainties for clear waters

The relative R_{rs} uncertainties, for each pre-defined Chl_{OCI} level, of both SeaWiFS and MODISA are shown in Fig. 6 and listed in Table 2. For clarity, although all spectral bands are listed in Table 2, only the RGB bands are plotted in Fig. 6. Note that these uncertainties are not the γ values in Eq. (2), but the standard deviation terms (σ) of Eq. (1), and they provide a statistical measure for error probability around the mean. For example, for a normal distribution with a zero mean bias, an uncertainty value of 10% suggests that about 68% of the pixels have relative R_{rs} errors <10%. Note that although our focus was on the 3×3 median filtered R_{rs} data because the 3×3 pixelization noise would be mostly removed in the global data products, the sensitivity study using the raw R_{rs} data yielded near-identical results for MODISA and some small (but noticeable) uncertainty increases for SeaWiFS. This is due to the much higher signal-to-noise (SNR) of MODISA than SeaWiFS (Hu et al., 2012a).

An immediate conclusion from these results is that the ocean color mission goal of achieving R_{rs} absolute accuracy or uncertainties for the blue wavelengths (e.g., 443 nm) to within 5% for oligotrophic oceans (by definition, Chl ≤ 0.1 mg m^{-3}) has been met by both SeaWiFS and MODISA. This is a new finding that has never been

Table 2
R_{rs} uncertainty (in %) of SeaWiFS and MODISA measurements in the North Atlantic (NA) and South Pacific (SP). The uncertainties are estimated as one standard deviation of relative errors (between R_{rs} and $R_{rs,true}$) of all qualifying pixels (σ of Eq. 1). The numbers listed in parentheses represent the mean absolute relative errors (MAREs) of all qualifying pixels (γ in Eq. 2). The MAREs or their equivalents (e.g., |RPD| in Antoine et al., 2008; MPD in Bailey and Werdell, 2006) have been used in the literature to represent R_{rs} uncertainties. Note that in this assessment, in order to minimize the impact of instrument digitization round−off and noise (Hu et al., 2001), R_{rs} data are first filtered using a 3×3 median, and then compared with $R_{rs,true}$. These relative uncertainties are presented in graphical forms in Fig. 6, where results without median filtering are also shown (dashed lines). Similar to Table 1, each pre-defined Chl level was allowed to cover a ±2% interval, and a sensitivity test showed that the tabulated results were insensitive to changes in this interval.

Chl (mg m^{-3})		0.03	0.05	0.1	0.15	0.2
SeaWiFS_NA	412	2.6(2.9)	4.9(4.6)	6.5(6.0)	8.8(7.0)	14.6(12.1)
	443	2.4(3.1)	3.4(3.5)	5.0(5.2)	8.4(6.7)	13.4(10.9)
	490	3.9(4.7)	4.9(5.1)	6.3(6.7)	10.8(8.4)	15.6(12.0)
	510	6.5(8.2)	8.3(8.9)	9.5(10.5)	14.1(11.2)	18.4(14.6)
	555	11.4(14.4)	13.8(15.1)	13.9(16.0)	17.2(14.2)	23.0(18.7)
	670	35.6(44.5)	41.9(45.9)	37.9(43.6)	46.6(37.1)	68.0(48.9)
SeaWiFS_SP	412	3.2(3.3)	4.2(4.2)	6.0(5.2)	9.9(12.2)	N/A
	443	2.1(3.6)	3.7(4.1)	5.4(4.7)	9.7(12.2)	N/A
	490	3.1(5.8)	7.3(7.4)	7.3(6.3)	12.3(14.0)	N/A
	510	5.2(10.7)	10.4(11.3)	10.3(9.1)	16.1(18.9)	N/A
	555	8.5(18.5)	13.5(16.8)	15.7(14.0)	21.5(25.4)	N/A
	670	22.0(48.3)	31.4(40.0)	47.4(38.0)	53.7(66.7)	N/A
MODIS_NA	412	2.9(2.2)	4.9(4.2)	6.2(7.2)	8.2(7.9)	12.2(9.8)
	443	2.1(1.6)	2.6(2.1)	3.9(5.2)	7.5(7.8)	10.9(8.4)
	488	2.8(2.2)	3.6(2.9)	4.8(6.6)	9.4(9.7)	13.7(9.9)
	531	7.4(5.8)	8.3(6.7)	9.1(12.9)	14.0(14.7)	16.9(12.9)
	547	9.4(7.3)	9.6(7.6)	10.0(13.9)	15.1(15.8)	17.8(13.7)
	667	25.2(19.4)	24.5(19.7)	21.3(23.6)	25.2(21.7)	25.7(20.1)
	678	22.6(17.7)	24.8(20.1)	21.1(21.3)	24.2(19.9)	25.2(19.5)
MODIS_SP	412	3.5(2.8)	4.2(4.0)	6.3(5.6)	12.7(11.3)	N/A
	443	2.1(2.0)	3.3(3.0)	4.8(4.1)	10.9(9.3)	N/A
	488	3.6(3.5)	6.4(5.8)	6.7(5.5)	13.2(10.8)	N/A
	531	7.6(7.4)	10.7(9.9)	11.2(9.6)	20.0(17.0)	N/A
	547	9.0(8.7)	11.7(11.0)	12.7(10.9)	21.9(18.8)	N/A
	667	21.8(19.4)	21.2(17.9)	28.3(23.3)	37.0(31.7)	N/A
	678	22.3(19.2)	20.8(17.4)	26.1(21.7)	32.9(28.7)	N/A

reported using in situ validations due to 1) lack of sufficient in situ measurements for oligotrophic waters and 2) difficulties in separating uncertainties in the in situ R_{rs} data from those in the satellite R_{rs} data. These difficulties have now been overcome with repeated satellite measurements over the same oligotrophic oceans and the use of a novel method to find the referencing $R_{rs,true}$ values. On the other hand, the results also indicate that R_{rs} uncertainties in the blue wavelengths can exceed the 5% goal for Chl > 0.1 mg m^{-3}, and are > 10% in the green and > 20% in the red for most of the time.

For both NA and SP, most of the SeaWiFS R_{rs} uncertainties are higher than those of MODISA, which could be explained by the increased SNR (or sensitivity) from SeaWiFS to MODISA (Hu et al., 2012a). It appears that the increases in SNR not only reduced pixelization noise, but also led to reduced R_{rs} uncertainties even after these noises were removed.

The R_{rs} uncertainties in reflectance units are presented in Fig. 7 and tabulated in Table 3. The same cross-sensor and cross-ocean differences as shown in Fig. 6 are observed for these absolute uncertainties, for example MODISA showed lower uncertainties than SeaWiFS for the same region. For oligotrophic waters (Chl ≤ 0.1 mg m^{-3}), the R_{rs} uncertainties are relatively stable (i.e., do not change with Chl). However, they tend to increase with increasing Chl for more productive waters, possibly due to increased aerosol variability for these waters (Cropp et al., 2005). Note that in the review paper by Gordon (1997) on the atmospheric correction of modern ocean color sensors, surface reflectance uncertainties in the blue (ρ_w(443)) due to atmospheric correction errors were estimated to be within ±0.002, corresponding to about ±0.0006 sr^{-1} in R_{rs}(443). The results in Fig. 7 show that nearly all R_{rs}(443) uncertainties are within this range, and for Chl ≤ 0.1 mg m^{-3} (the practical definition for oligotrophic waters) they are significantly lower. Clearly, excellent performance has been achieved for both SeaWiFS and MODISA through continuous improvement in both sensor calibration and algorithm refinement.

4. Discussion

4.1. Interpretation of R_{rs} uncertainties

Although the calculation of the various uncertainty estimates, after the establishment of the methodology, is straightforward, interpretation of the results is not. In the published literature, MPD (γ from Eq. 2 or its equivalent) has often been used to represent the absolute accuracy or the uncertainty (e.g., Antoine et al., 2008; Werdell and Bailey, 2005). However, by its literal meaning uncertainty should be a measure of probability of how close a given R_{rs} is to the "truth." Thus, the standard deviation term may be a better measure of uncertainty, as for a normal error distribution ~68% of the data points would have errors within 1 standard deviation and ~95% of the data points would have errors within 2 standard deviations around the mean bias. Indeed, most results showed an error distribution close to normal with a mean bias close to 0 (mean bias within ±0.0002 sr^{-1} for most cases for the blue and green bands and within ±0.00005 sr^{-1} for the red bands). Even though, both measures show comparable results, as listed in Tables 2 and 3 (the standard deviations are listed in the tables, with γ of Eq. 2 and Γ of Eq. 4 listed in the parentheses). Thus, both measures may be regarded as valid.

All results were obtained from thousands of data files for the entire year of 2006. Can they be generalized for other years? A sensitivity test using data covering the same areas but from 2004 showed nearly identical results for $R_{rs,true}$ (<1% for the blue and green bands) and very similar results for the R_{rs} uncertainties. Thus, we believe that the results listed here can be interpreted for other years as well. Likewise, the individual Chl levels were allowed to cover a ±2% range in order to find enough pixels for statistical analyses. A sensitivity test using a ±5% Chl range showed virtually no difference for all green and red wavelengths (<1%), and negligible difference for the blue wavelengths (<4%). This is because that R_{rs} in the green and red is insensitive to Chl changes (Fig. 4). Indeed, errors in Chl_{OCI} due to atmospheric correction residual errors are <5% for most cases (Figs. 10 and 11 in Hu et al., 2012b), confirming the validity of the results presented here.

However, the statistical results here are based on the Level-2 pixels at original resolutions. Most researchers in the ocean color community have used composite data, after data binning in both space and time, for time series analyses. These include the 4-km resolution or 9-km resolution monthly or 8-day composite data. Correspondingly, one pixel in these global composite data may be an average of 10–100 Level-2 pixels after considering cloud cover and other artifacts. Then, are the results shown here still valid for these global composite data?

One way to test such validity is to examine the binned data and compare with those without binning. For this purpose, all valid SeaWiFS pixels for the NA were binned into 4×4 (16×) and 8×8 (64×) groups, respectively. The use of 16-pixel groups is to simulate a 4-km binned daily data product, while the use of 64-pixel groups is to simulate a 4-km binned monthly data product (assuming 4 cloud-free days in a given month, as on average only 10–15% of all collected data are valid, Maritorena et al, 2010). For each 4×4 (or 8×8) group, a standard deviation (σ) of relative errors (δ of Eq. 1, gauged against $R_{rs,true}$) within the group was derived. The mean and standard deviation of σ's from all these 4×4 (or 8×8) groups were derived and presented in Fig. 8a–c. The mean σ (solid points in Fig. 8) represents, on average, how much R_{rs} uncertainty an individual group (4×4 or 8×8) may contain while the standard deviation of σ (error bars in Fig. 8) represents how much R_{rs} uncertainty from one

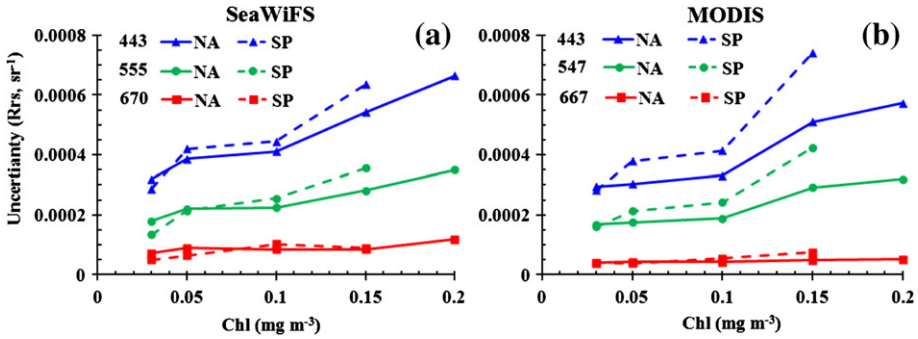

Fig. 7. Absolute uncertainties (in R_{rs} units, Ω of Eq. 3) of SeaWiFS and MODISA R_{rs} data for the North Atlantic (NA) and South Pacific (SP). The x-axis is Chl_{OCI}. About 68% of the non-flagged (i.e., valid) pixels have R_{rs} errors (gauged against the corresponding $R_{rs,true}$) less than the uncertainties. R_{rs} noise has been removed using a 3×3 median filter before uncertainty calculations. Data are listed in Table 3.

group differs from other groups. As a comparison, the σ value of R_{rs} errors from the original data (without binning) is also shown in Fig. 8a–c. Clearly, except for one case (R_{rs}(670), Chl = 0.03 mg m^{-3}), all statistical measures are nearly identical, suggesting that the uncertainty estimates from the original Level-2 pixels can be used to interpret uncertainties in the binned data. Another test using one year (2006) of the SeaWiFS Level-3 global monthly data products of R_{rs} at 9-km resolution (also obtained from NASA OBPG) showed very similar results to those shown in Fig. 8, thus confirming the findings from these simulations.

4.2. Origin of the R_{rs} errors

For a perfectly calibrated instrument where the top-of-atmosphere (TOA) radiance or reflectance is error free, the only error source in the satellite-derived R_{rs} data is the imperfect atmospheric correction (including correction for other environmental perturbations such as whitecaps and sun glint). Because most (>90%) of the TOA signal over clear waters comes from the atmosphere, a small error in the atmospheric correction would translate to a much larger relative error in the derived R_{rs}. After considering all potential error sources in the atmospheric correction, Gordon (1997) estimated an error budget of $<\pm 0.0006$ sr^{-1} for R_{rs}(443). Fig. 7 shows that nearly all R_{rs}(443) uncertainties are within this range, suggesting that most of these uncertainties could originate from the atmospheric correction residual errors. To test this speculation, all pixels were partitioned into different groups according to their aerosol optical properties (τ and α), with R_{rs} uncertainties estimated for each partition. Some examples for SeaWiFS R_{rs}(555) and MODISA R_{rs}(547) are presented in Fig. 9. Although the impact of α is not apparent, higher τ did lead to higher R_{rs} uncertainties, consistent with results from atmospheric correction simulations (Gordon, 1997). The same argument may also explain the higher R_{rs} uncertainties for Chl > 0.1 than those for Chl ≤ 0.1 mg mg^{-3}, as waters with high biomass in these areas are often associated with more aerosols (Cropp et al., 2005).

The calibration of any ocean color sensors, of course, is never perfect. Indeed, a critical requirement is the vicarious calibration or the self-tuning of the sensor-algorithm system. In the vicarious calibration the sensor's radiometric gains are adjusted using a variety of techniques including ground measurements, multi-sensor consistency checks, and constraints on the spectral shapes (Eplee et al, 2001; Franz et al., 2007; Gordon, 1998; Stumpf and Werdell, 2010; Werdell et al., 2007). In all these techniques the sensor gain for the near-infrared band (869-nm for MODISA and 865-nm for SeaWiFS)

Table 3
Same as Table 2, but the uncertainties are presented in R_{rs} units. These are presented in graphical form in Fig. 7. As in Table 2, R_{rs} data are first filtered using a 3×3 median, and then compared with $R_{rs,true}$.

Chl (mg m^{-3})		0.03	0.05	0.1	0.15	0.2
SeaWiFS_NA	412(×10^{-4} sr^{-1})	4.44(5.04)	6.92(6.42)	6.10(5.69)	6.16(4.91)	7.88(6.53)
	443(×10^{-4} sr^{-1})	3.19(4.22)	3.87(3.92)	4.11(4.28)	5.43(4.33)	6.65(5.41)
	490(×10^{-4} sr^{-1})	2.93(3.56)	3.34(3.54)	3.72(3.94)	5.64(4.42)	6.60(5.06)
	510(×10^{-4} sr^{-1})	2.47(3.10)	3.01(3.25)	3.26(3.59)	4.66(3.70)	5.31(4.22)
	555(×10^{-4} sr^{-1})	1.80(2.27)	2.20(2.40)	2.25(2.58)	2.82(2.33)	3.50(2.84)
	670(×10^{-5} sr^{-1})	7.16(8.96)	8.89(9.75)	8.49(9.76)	8.54(6.80)	11.88(8.54)
SeaWiFS_SP	412(×10^{-4} sr^{-1})	5.88(5.95)	6.24(6.22)	6.08(5.31)	7.97(9.83)	N/A
	443(×10^{-4} sr^{-1})	2.87(4.87)	4.20(4.62)	4.45(3.90)	6.35(8.02)	N/A
	490(×10^{-4} sr^{-1})	2.28(4.31)	5.06(5.17)	4.33(3.73)	6.52(7.46)	N/A
	510(×10^{-4} sr^{-1})	1.93(3.97)	3.83(4.17)	3.66(3.24)	5.55(6.50)	N/A
	555(×10^{-4} sr^{-1})	1.34(2.91)	2.15(2.67)	2.55(2.27)	3.56(4.22)	N/A
	670(×10^{-5} sr^{-1})	4.95(10.87)	6.49(8.27)	10.27(8.24)	8.96(11.12)	N/A
MODIS_NA	412(×10^{-4} sr^{-1})	4.96(3.75)	7.01(5.98)	6.16(7.10)	6.01(5.78)	6.81(5.45)
	443(×10^{-4} sr^{-1})	2.95(2.26)	3.04(2.43)	3.31(4.42)	5.10(5.29)	5.72(4.39)
	488(×10^{-4} sr^{-1})	2.25(1.78)	2.60(2.08)	3.01(4.10)	5.26(5.43)	6.21(4.48)
	531(×10^{-4} sr^{-1})	1.83(1.44)	2.03(1.63)	2.26(3.19)	3.51(3.69)	3.88(2.95)
	547(×10^{-4} sr^{-1})	1.68(1.31)	1.75(1.40)	1.88(2.62)	2.92(3.06)	3.20(2.47)
	667(×10^{-5} sr^{-1})	3.97(3.05)	4.23(3.40)	4.22(4.69)	4.84(4.17)	5.13(4.02)
	678(×10^{-5} sr^{-1})	3.41(2.67)	4.15(3.36)	4.09(4.14)	4.62(3.81)	5.52(4.28)
MODIS_SP	412(×10^{-4} sr^{-1})	6.55(5.20)	6.38(6.08)	6.71(6.02)	10.43(9.32)	N/A
	443(×10^{-4} sr^{-1})	2.82(2.70)	3.79(3.51)	4.14(3.55)	7.42(6.32)	N/A
	488(×10^{-4} sr^{-1})	2.82(2.74)	4.64(4.15)	4.19(3.44)	7.33(5.97)	N/A
	531(×10^{-4} sr^{-1})	1.85(1.80)	2.60(2.42)	2.83(2.42)	5.03(4.26)	N/A
	547(×10^{-4} sr^{-1})	1.61(1.56)	2.13(2.00)	2.42(2.08)	4.24(3.65)	N/A
	667(×10^{-5} sr^{-1})	4.01(3.58)	3.88(3.29)	5.43(4.48)	7.53(6.44)	N/A
	678(×10^{-5} sr^{-1})	3.95(3.40)	3.73(3.12)	5.24(4.35)	7.00(6.10)	N/A

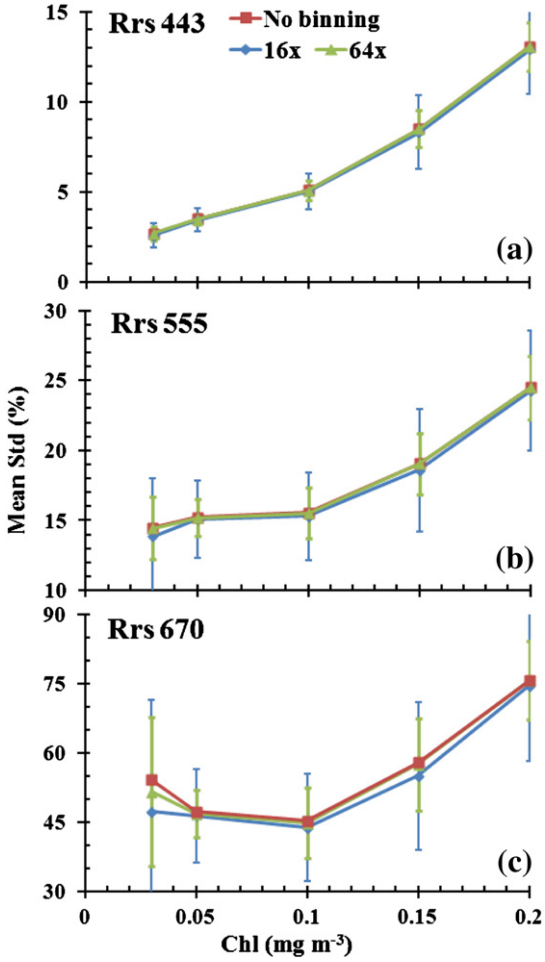

Fig. 8. Impacts of data binning on SeaWiFS R_{rs} uncertainty estimates. For each Chl_{OCI} value (x-axis), all qualified valid pixels in the North Atlantic are divided into 4×4 (16×) groups. For each group, a standard deviation (Std) of relative errors from all pixels in that group, gauged against $R_{rs,true}$, is estimated. The mean and standard deviation of these Stds for all groups are presented in (a)–(c). The same procedure is repeated for the 8×8 (64×) groups. Also shown in the figures are the results ("no binning") from the original Level-2 data calculations without median filtering (red curves; these are identical to the dashed black curves in Fig. 6a–c).

has never been adjusted (i.e., the pre-launch gain was assumed accurate), and the success of the calibration has been evaluated using in situ validations of the derived R_{rs} (or L_{wn}). Currently, the vicarious gains used operationally in the SeaDAS software package were derived from the long-term in situ measurements from the marine optical buoy (MOBY, Clark et al., 1997). Different calibration approaches could result in differences in the vicarious gains by up to ±0.9% (Werdell et al., 2007). Such a difference for a specific band would create a systematic bias in the retrieved R_{rs} but unlikely in the standard deviations. Small changes in vicarious gains will change the $R_{rs,true}$ values in Table 1 and R_{rs} values from individual pixels in a similar manner, with R_{rs} uncertainty estimates in Table 3 virtually unchanged. This is because that the $R_{rs,true}$ values used as the references to determine the R_{rs} uncertainties are derived from satellite instead of in situ measurements. In contrast, if in situ R_{rs} were used as the references in Table 1, $R_{rs,true}$ values would be independent to vicarious gains, but R_{rs} from individual pixels and R_{rs} uncertainties in Table 3 would change with vicarious gains. Thus, R_{rs} uncertainties in Table 3 are insensitive to vicarious gain changes, and the monotonous spectral relationships between the R_{rs} errors (Fig. 10, Section 4.3, i.e., $R_{rs}(443)$ errors ≈ 2×$R_{rs}(555)$ errors ≈ 4×$R_{rs}(670)$ errors) suggest that most R_{rs} errors originated from atmospheric correction algorithms rather than from the vicarious calibration. Even if the NIR (869 and 865 nm) vicarious gains are adjusted, most of the effect will be compensated by the atmospheric correction algorithms (Wang and Gordon, 2002), leading to minimal impacts on the retrieved R_{rs}.

Can the imperfect empirical Chl algorithms contribute to some of the R_{rs} estimates, as they were used to find the constraint to determine $R_{rs,true}$? Neither the band-ratio OCx algorithm nor the band-subtraction OCI algorithm was designed to separate in-water perturbations by CDOM or detrital particles, yet in different ocean basins these non-Chl constituents may have different impacts on empirical algorithms (Dierssen, 2010; Szeto et al., 2011). As a result, the same algorithm may work well for one ocean basin but perform poorly for another when identical algorithm coefficients are used (Szeto et al., 2011). However, the purpose of the use of Chl_{OCX} and Chl_{OCI} in this work is only to find a constraint as opposed to finding the absolute Chl value. As long as the impacts of variable CDOM and detrital particles from the same ocean gyre on the two algorithms are similar (this has been proven through simulations in Hu et al., 2012b), the argument of using the constraint and the approach to determine $R_{rs,true}$ should be both valid. Even if both Chl_{OCx} and Chl_{OCI} are wrong (in the same directions), the consequence would be a slight shift on the x-axis of Figs. 4–9, thus having little impact on the major findings here ($R_{rs,true}$ and R_{rs} uncertainties). In the worse-case scenario when Chl_{OCx} and Chl_{OCI} are incorrect in the opposite directions (one overestimated and the other underestimated), the consequence would be a slight shift on both the x-axis and y-axis of Figs. 4–9, causing errors in the estimates of the $R_{rs,true}$ and R_{rs} uncertainties. However, both in situ data regression and model simulations

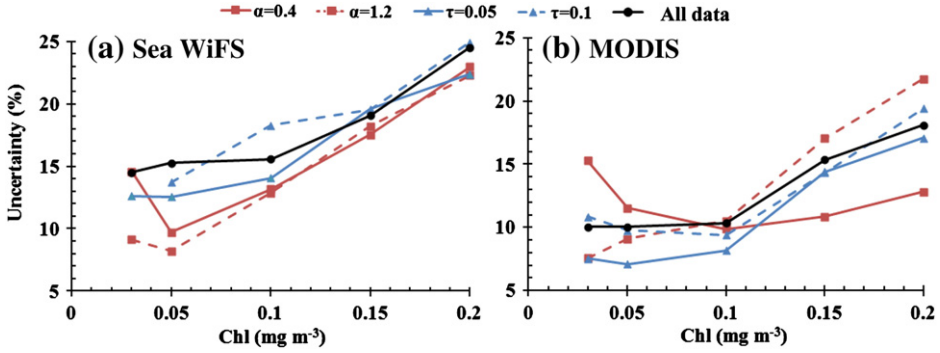

Fig. 9. Impacts of aerosol properties on the uncertainties of SeaWiFS $R_{rs}(555)$ and MODISA $R_{rs}(547)$ in the North Atlantic. The x-axis is Chl_{OCI}. Data used in these calculations are the original R_{rs} data without median filtering. The results show that although the impact of the angstrom exponent (α, a measure of the aerosol scattering spectral slope or aerosol type) is not apparent, higher aerosol optical thickness (τ, at 865 nm for SeaWiFS and 859 nm for MODISA) would lead to higher R_{rs} uncertainties. In the data partitioning, once a parameter is fixed, there is no more constraint on all other parameters.

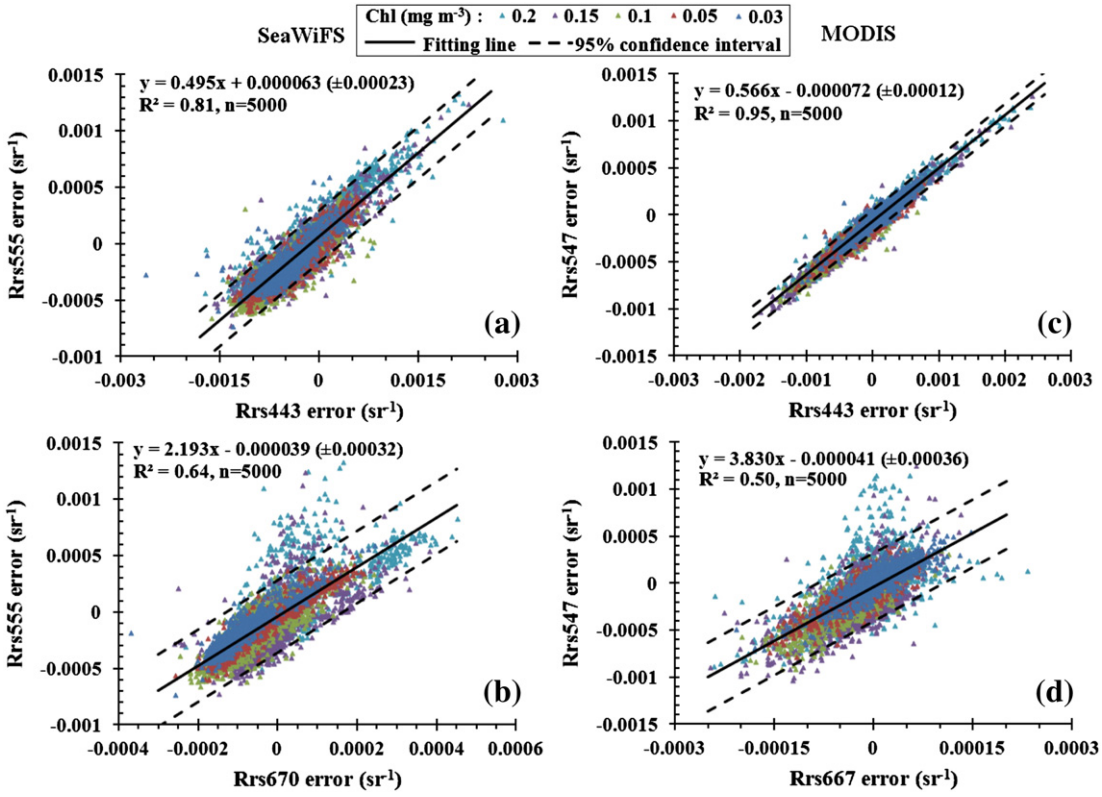

Fig. 10. Spectral relationships between R_{rs} errors (not uncertainty) of SeaWiFS and MODISA bands, derived from data collect over the North Atlantic. The errors are determined as the relative difference between R_{rs} (after 3×3 median filtering to remove digitization round off and instrument noise) and $R_{rs,true}$. The dashed lines are the 95% confidence intervals, represented by the intercept values in the parentheses.

showed that this situation is unlikely (Hu et al., 2012b), and small errors in the algorithm coefficients in either the OCx or the CI would lead to small shifts in the y-axis as opposed to significant changes in the findings. Indeed, even though the absolute Chl_{OCI} values in the NA and SP cannot be both right due to different CDOM influence (Szeto et al., 2011), $R_{rs,true}$ derived from the two ocean basins still showed excellent agreement for both SeaWiFS and MODISA for all but the 412-nm bands (Fig. 5), thus strongly supporting the above arguments. Likewise, because the algorithm coefficients of both OCx and CI were tuned using global data, both Chl_{OCx} and Chl_{OCI} may be overestimated in the NA and underestimated in the SP due to the different CDOM influence (more CDOM in the NA than in the SP, as $R_{rs}(412)$ in SP is always higher than in NA for the same Chl_{OCI} value, Fig. 5d–e) yet these over- or underestimates would only result in a slight shift in the x-axis and thus would not change the uncertainty estimates significantly. However, the absolute accuracy in such derived $R_{rs,true}$ values still requires validation using high-quality in situ measurements.

4.3. Implication for uncertainty estimates for other products

All R_{rs} uncertainty estimates from the literature (including this current study) are based on statistics of large datasets. On the other hand, it is desirable to have an uncertainty estimate on every image pixel. Such an uncertainty "product" is not available in either the Level-2 or the Level-3 data products from the NASA operational processing. Clearly, this is not a trivial task, although some recent attempts have been made toward this direction.

Wang, P., et al. (2005) used an ensemble of IOP solutions for a given input R_{rs} spectrum to estimate the uncertainties in the IOPs, which were derived from a linear matrix inversion algorithm (Hoge and Lyon, 1996). A solution was found once the IOP-modeled R_{rs} agreed with the input R_{rs} to within 10% for all spectral bands. The statistics of all IOP solutions (>1000) provided a measure of IOP uncertainties. Implementing the approach for pixel-wise image processing is computationally expensive, and the uncertainties in the input R_{rs} were unknown although they were assumed to be 3% according to the field measurements by Chang et al. (2003).

Lee et al. (2010) showed an analytical method on how to estimate IOP uncertainties from an input R_{rs} spectrum using a quasi-analytical inversion algorithm (QAA, Lee et al., 2002). However, although the uncertainties due to parameterization of the inversion models have been documented (Lee et al., 2004; Park and Ruddick, 2005; Zaneveld et al., 2005), the input R_{rs} was assumed error free because of lack of information on the R_{rs} uncertainties on every pixel even though average uncertainties have been estimated using in situ validation statistics (e.g., Antoine et al., 2008; Bailey and Werdell, 2006; Zibordi et al., 2002). When the R_{rs} uncertainties are available pixel-wise, they can be incorporated following the theory of error propagation for the generation of IOP uncertainty maps.

The results of this study make it possible to incorporate R_{rs} uncertainties in the IOP inversion models for every clear-water pixel. Fig. 10 shows that the R_{rs} errors are not spectrally independent, but significantly correlated between all bands. Thus, if an R_{rs} error is known from a reference band (e.g., 670 or 555 nm), R_{rs} errors in other bands can be derived from the statistical relationships with the 95% confidence levels bounding the uncertainties. For example, $R_{rs}(555)$ or $R_{rs}(547)$ errors are about half of $R_{rs}(443)$ errors for both SeaWiFS and MODISA. This result agrees well with the model simulations assuming maritime aerosols (Fig. 9b of Hu et al., 2012b). Because of the stability of $R_{rs}(555)$ (or $R_{rs}(547)$) for clear waters (Gordon and Clark, 1981; Morel and Maritorena, 2001), this band might be chosen as a reference, whose R_{rs} errors may be derived from the established $R_{rs,true}$ value for a particular ocean region. The implementation of such a pixel-wise uncertainty estimation scheme, however, requires further work to derive the $R_{rs,true}(555)$ values for all clear waters ($Chl_{OCI} \leq 0.25$ mg m^{-3}). In

practice, such derivation may need to be carried out for each oceanographic province because of the backscattering and CDOM variability across ocean basins (Dierssen, 2010; Huot et al., 2008; Szeto et al., 2011). The influence of both backscattering and CDOM decreases with increasing wavelengths, suggesting that using a longer wavelength (e.g., 670 nm) as the reference might be a better choice (see Section 4.5). Currently, before a pixel-wise uncertainty estimation scheme is implemented, the statistical relationships as well as the error distributions in Fig. 10 can at least be incorporated immediately in the Lee et al. (2010) approach to refine the IOP uncertainty estimates for large oceanographic regions.

4.4. Implication for future ocean color missions

Studies of ocean's biogeochemical changes in response to climate variability can only be achieved through continued and consistent observations from multiple missions, as satellite missions are typically designed for a 5-year lifespan even though they could last longer (e.g., 1997–2010 for SeaWiFS; 2002–present for MODISA). To continue these observations, the U.S. NASA is planning for an ocean ecosystem sensor as part of the Pre-Aerosol-Clouds-Ecosystems (PACE) mission with a scheduled launch date in 2019 (NASA, 2010). In addition, NASA is also planning three tier 2 Decadal Survey missions (NRC, 2007): 1) ACE; 2) Geostationary Coastal and Air Pollution Events (GEO-CAPE, Fishman et al., 2012); and (3) Hyperspectral Infrared Imager (HyspIRI), each with ocean color capability. The question is then what could be learned from the findings here in order to help design these future sensors and help define their technical goals.

First, the mission goals of accurate R_{rs} retrievals need to be specified more clearly. The original specification for SeaWiFS (Hooker et al., 1992) called for an accuracy of "water-leaving radiances to within 5% absolute." The results in Table 2 and Fig. 6 show that this goal can only be achieved for the blue bands for oligotrophic waters ($Chl \leq 0.1$ mg m^{-3}). Even though, the uncertainty values only provide a probability of error statistics, with some small portion of the data exceeding the 5% goal. In the green bands, the errors in the absolute accuracy and the relative uncertainties become significantly larger. Hence, a more precise way to define the mission goal may be: to achieve less than 5% uncertainties in the retrieved remote sensing reflectance in the blue bands and less than 15% in the green bands for oligotrophic waters. Further, the relative uncertainties (Fig. 6) change with the $R_{rs,true}$ values (the denominator of the relative term, Fig. 5) even though the uncertainties (in sr^{-1}, the numerator of the relative term, Fig. 7) are stable for $Chl \leq 0.1$ mg m^{-3}. An alternative, and clearer, way to define this mission goal is then to specify uncertainties in the absolute R_{rs} units.

Second, each mission will require an error tolerance estimate for the specific science goals. For example, one science goal of the GEO-CAPE mission (Fishman et al., 2012) is to study the short-term (diurnal) ocean changes in selected coastal regions. What R_{rs} errors can be tolerated in order to detect biogeochemical changes during the course of a day with repeated measurements from a geo-stationary platform? The R_{rs} uncertainty estimates in Table 3 and Fig. 7 provide the lower bounds for the tolerance studies when combined with inversion algorithms (e.g., Lee et al., 2002, 2010). This is because that the estimates were obtained from the best-case scenarios in two oligotrophic gyres away from land. For coastal waters, the absolute R_{rs} uncertainties can only be higher due to more problems in atmospheric correction and in-water perturbations. Thus, the tabulated values provide a reference for future studies on error tolerance.

Third, sensor design requires specifications on SNR and maximum radiance (Hu et al., 2012a). Higher SNR will lead to less pixelization noise in the data products. Although most of the noise can be removed through data binning, the results here showed generally higher R_{rs} uncertainties for SeaWiFS than for MODISA. We believe that this difference resulted primarily from their different SNRs. The difference may have a significant impact on the global data analyses. Higher R_{rs} uncertainties indicate more data spread around the $R_{rs,true}$ values (Fig. 4). The spread was not treated equally, however. For example, there is a significant portion of the negative spread (i.e., the points below the green curve in Fig. 4b, where the cut-off R_{rs} threshold is about 0.0008 sr^{-1}) that has been removed by the "LOWLW" flag during the global data binning. Therefore, more data spread (as with SeaWiFS) will lead to more

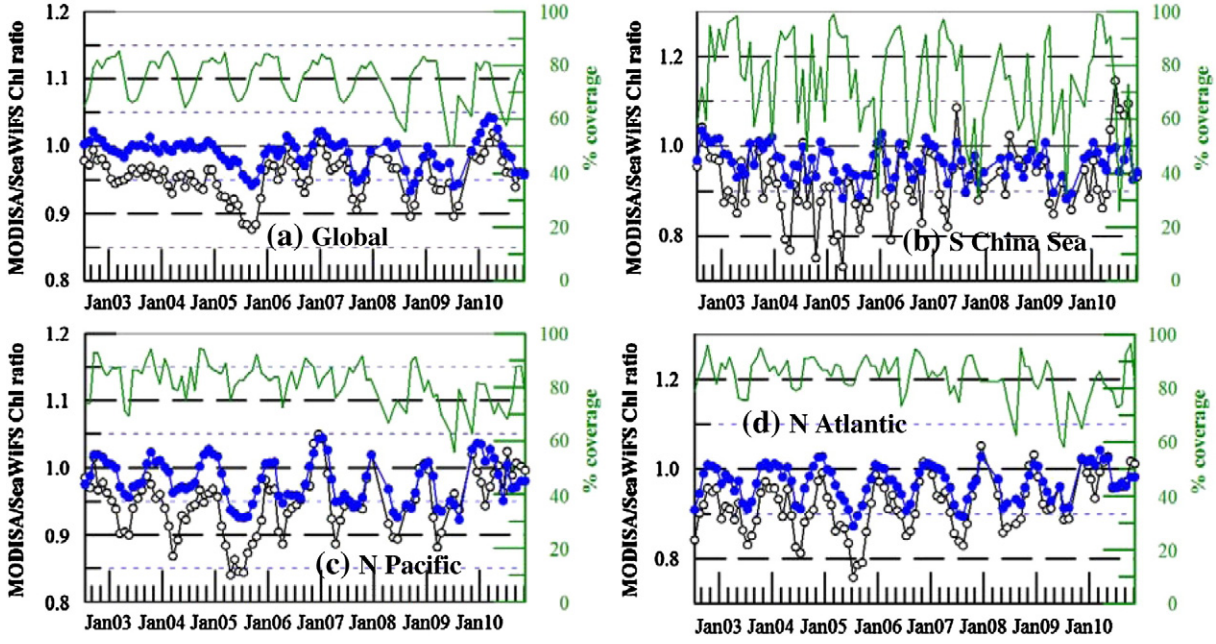

Fig. 11. Monthly mean Chl ratio of MODISA/SeaWiFS over open oceans (>1000 m). Black empty symbols are for the OCx algorithm, and blue solid symbols are for the OCI algorithm. For each region, the statistics were calculated from identical non-flagged 9-km daily pixels from SeaWiFS and MODISA. The percentage coverage indicates the ratio between non-flagged pixels for the particular month and non-flagged pixels for the SeaWiFS mission climatology.

positively-biased data binning. We believe that this could explain why MODISA global mean Chl (over oligotrophic oceans) was generally lower than SeaWiFS (Hu et al., 2012b, Fig. 11 black curves). Thus, to reduce potential biases, it is desirable to have SNRs comparable to MODISA.

Finally, although it is not a direct conclusion from the results shown above, this study was not possible without the recently developed Chl_{OCI} algorithm, which provided a constraint to determine the $R_{rs,true}$ values. Application of the new algorithm to global SeaWiFS and MODISA data showed significant improvement in cross-sensor consistency (Hu et al., 2012b; Fig. 11). Indeed, large differences are often found between SeaWiFS and MODISA default Chl_{OCx}, as shown by the black curves in Fig. 11. In certain months and ocean basins, the differences could reach 10–20%, comparable or larger than decadal ocean changes derived from single- or multi-sensor studies (Antoine et al., 2005; Gregg and Casey, 2004, 2010). Although the exact reasons of these large differences are still unclear (we speculate that they originated from the different SNRs; see argument above), they created difficulties in time-series analyses: if one dataset shows a temporal change while the other does not, which one shall we trust? In contrast, the new Chl algorithm led to significantly reduced differences between SeaWiFS and MODISA (blue curves in Fig. 11), thus providing a more consistent data series between difference sensors. In the future if only one sensor is available, more confidence will be gained in data continuity and consistency when the new Chl algorithm is used to generate data products for blue waters at multi-decadal scales.

4.5. Reduce R_{rs} uncertainties through empirical correction

Although cross-sensor consistency in the Chl data products can be improved through the new Chl_{OCI} algorithm because the algorithm is less sensitive than the Chl_{OCx} algorithms to R_{rs} errors, other data products still suffer from the R_{rs} errors. While the ultimate way to remove or reduce these errors is through improved algorithms for correction of the atmospheric effects and other perturbations (e.g., sun glint, whitecaps), a simple empirical correction may be achieved through the use of the established $R_{rs,true}(670)$ and $R_{rs,true}(667)$ values (Table 1) together with the spectral relationships between R_{rs} errors (Fig. 10).

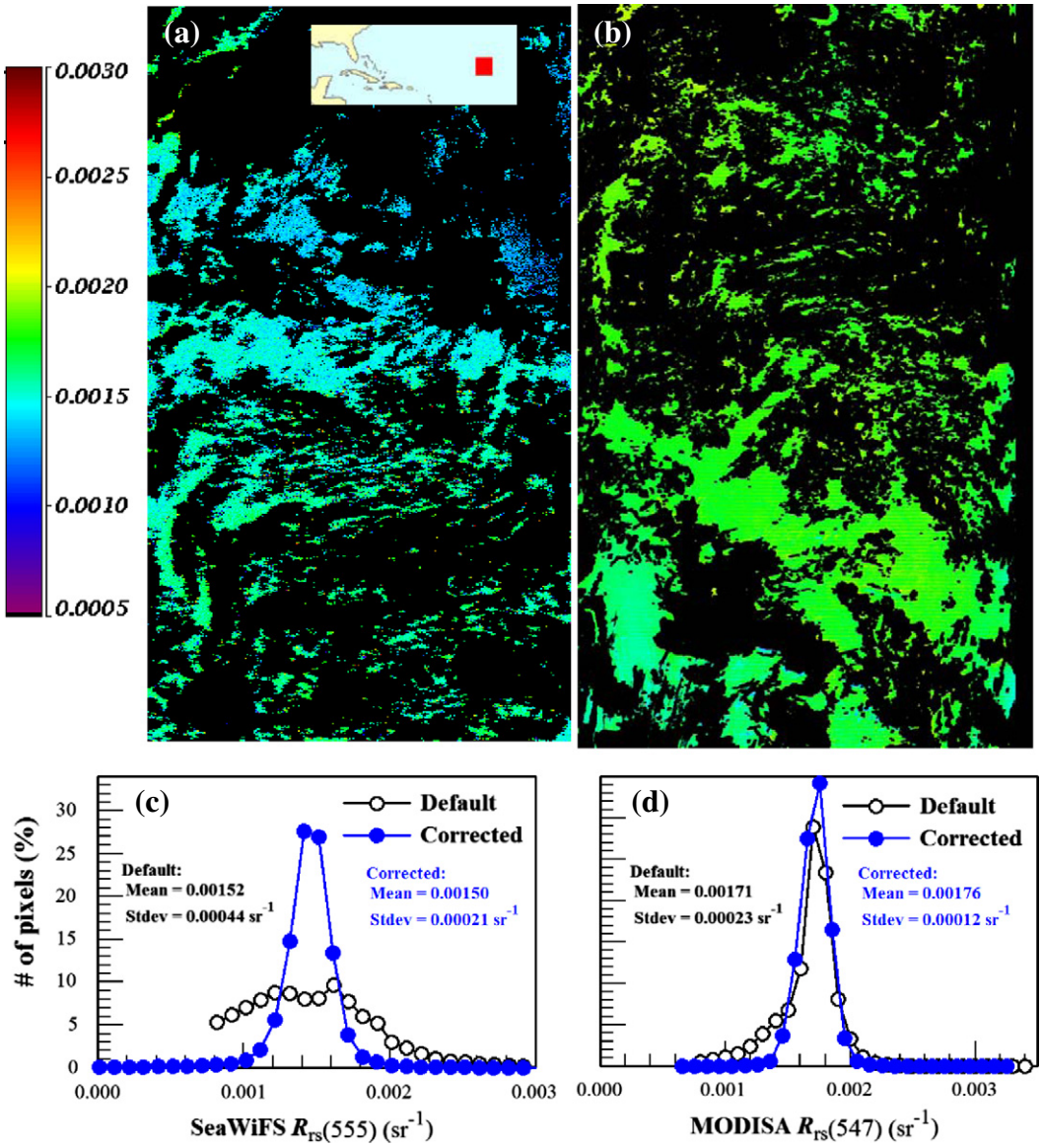

Fig. 12. (a) SeaWiFS $R_{rs}(555)$ (sr^{-1}) after empirical correction using Eqs. (5)–(7). The image corresponds to the original image shown in Fig. 1a. (b) MODISA $R_{rs}(547)$ (sr^{-1}) after the same empirical correction but with coefficients adjusted for MODISA. The image corresponds to the original image shown in Fig. 1b. The graphs in (c) and (d) show histograms of the original (i.e., default) and corrected R_{rs} values.

An example of such a correction on SeaWiFS $R_{rs}(555)$ and MODISA $R_{rs}(547)$ from the image pair in Fig. 1 is shown in Fig. 12. For SeaWiFS, $R_{rs,true}(670)$ for the entire image was assumed to be the mean $R_{rs,true}(670)$ for all Chl levels of Table 1. This pixel-independent constant was then used to derive the $R_{rs}(670)$ error for every pixel as

$$\Delta R_{rs}(670) = R_{rs}(670) - R_{rs,true}(670), \quad (5)$$

where $R_{rs}(670)$ is from the pixel of consideration. Then, $R_{rs}(555)$ error for the pixel was estimated as (Fig. 10b)

$$\Delta R_{rs}(555) = f(\Delta R_{rs}(670)) = 2.193\Delta R_{rs}(670) - 0.000039, \quad (6)$$

and the corrected $R_{rs}(555)$ was derived as

$$R_{rs}^{corrected}(555) = R_{rs}(555) - \Delta R_{rs}(555). \quad (7)$$

The correction procedure was repeated for every valid SeaWiFS pixel in Fig. 1a, and the same procedure (with coefficients adjusted according to Table 1 and Fig. 10d) was applied to every valid MODISA pixel in Fig. 1b, with the corrected R_{rs} images for SeaWiFS and MODISA shown in Fig. 12a and b, respectively. Compared with the original R_{rs} images in Fig. 1, the corrected images show much reduced noise and smoother R_{rs} values, which are expected for the oligotrophic ocean gyre. Indeed, the corrected images show much tighter histograms around the mean values (Fig. 12c and d), with standard deviations (a measure of R_{rs} uncertainty) significantly reduced (about half) from the original values. Application of the correction procedure to other wavelengths showed similar improvements.

Can the empirical correction be applied globally to reduce R_{rs} uncertainties? This depends on 1) whether $R_{rs,true}(670)$ can be known a priori and 2) whether the spectral relationships between R_{rs} errors (Fig. 10) can be extended elsewhere. While for low-Chl waters $R_{rs,true}(670)$ appears stable, as shown in Fig. 5c, for higher-Chl waters especially turbid coastal waters $R_{rs,true}(670)$ may be highly variable. Likewise, for high-backscattering waters such as in the Southern Ocean it is also difficult to know $R_{rs,true}(670)$ a priori. However, for most of the clear waters (Chl $\leq$ 0.25 mg m^{-3}, representing ~78% of the global ocean), $R_{rs,true}(670)$ might be assumed a constant to provide a reference to assess $R_{rs}(670)$ errors for each pixel. The spectral relationships in Fig. 10 were derived from the N. Atlantic gyre where the aerosol scattering angstrom exponent varies between 0.6 and 1.0 according to 10 years of SeaWiFS data. Such a range represents about 70% of the global distributions (Fig. 11a of Hu et al., 2012b), suggesting that for most cases the empirical relationships between R_{rs} errors (Fig. 10) may be used. Even when the angstrom exponent is significantly different from 1.0 (e.g., it can reach 1.5 for tropospheric aerosols), a correction using the established relationships will still reduce the R_{rs} errors to some extent. We plan to implement such a correction scheme to test the sensitivities of other ocean color data products (e.g., IOPs) to the correction, with the ultimate purpose of improving multi-sensor consistencies in all data products.

5. Conclusion

Two fundamental difficulties in understanding the uncertainties of the satellite-derived R_{rs} data products are 1) the lack of reliable means to separate uncertainties in the in situ data from those in the satellite data, and 2) the lack of sufficient in situ data covering all possible satellite measurement scenarios. The application of a new Chl algorithm attempted to overcome these difficulties by focusing on a large volume of satellite data collected over two contrasting oligotrophic gyres and by providing a practical means to determine the "true" R_{rs}, used as references or surrogates of "ground truth" in the absence of error-free in situ measurements. The analyses were applied to both SeaWiFS and MODISA measurements, leading to several new findings, for example both sensors have met their mission goals of achieving R_{rs} uncertainties and absolute accuracy (assuming that the $R_{rs,true}$ values can represent the truth) to within 5% for blue bands and blue waters. The R_{rs} errors appear to be spectrally related, which provide constraints to empirically correct these errors over clear waters. The tabulated results provide complementary information to uncertainty estimates based on in situ measurements, as the latter are still required to evaluate the absolute accuracy of the $R_{rs,true}$ values for the individual Chl levels below 0.25 mg m^{-3} and to assess R_{rs} uncertainties for more productive waters. However, we believe that the results presented here will provide lower bounds for R_{rs} uncertainties over more productive waters, including turbid coastal waters, where both atmospheric and oceanic properties are more complex, and the findings here have significant implications for uncertainty estimates of other ocean color data products and for future mission design. We anticipate extending these analyses to other past and current ocean color sensors in the near future.

Acknowledgment

This work was supported by the University of South Florida, the U.S. NASA Ocean Biology and Biogeochemistry (OBB) program and the Water and Energy Cycle program, the Gulf of Mexico Research Initiative through the Center for Integrated Modeling and Analysis of the Gulf Ecosystem (C-IMAGE), and inspired by numerous discussions within the GEO-CAPE science definition team. Support of Lian Feng was provided by an education program for visiting and exchanging students. We thank the NASA OBPG for providing SeaWiFS and MODISA data, and Bryan Franz for implementing the new Chl algorithm to generate the global ocean color data. We also thank the two anonymous reviewers for providing comments and suggestions to improve the writing.

References

Ahmad, Z., Franz, B. A., McClain, C. R., Kwiatkowska, E. J., Werdell, J., Shettle, E. P., et al. (2010). New aerosol models for the retrieval of aerosol optical thickness and normalized water-leaving radiances from the SeaWiFS and MODIS sensors over coastal regions and open oceans. *Applied Optics*, *49*, 5545–5560.

Antoine, D., d'Ortenzio, F., Hooker, S. B., Bécu, G., Gentili, B., Tailliez, D., et al. (2008). Assessment of uncertainty in the ocean reflectance determined by three satellite ocean color sensors (MERIS, SeaWiFS and MODIS-A) at an offshore site in the Mediterranean Sea (BOUSSOLE project). *Journal of Geophysical Research*, *113*, C07013.

Antoine, D., Morel, A., Gordon, H. R., Banzon, V. F., & Evans, R. H. (2005). Bridging ocean color observations of the 1980s and 2000s in search of long-term trends. *Journal of Geophysical Research*, *110*, C06009.

Bailey, S. W., & Werdell, P. J. (2006). A multi-sensor approach for the on-orbit validation of ocean color satellite data products. *Remote Sensing of Environment*, *102*, 12–23.

Brown, C. A., Huot, Y., Werdell, P. J., Gentili, B., & Claustre, H. (2008). The origin and global distribution of second order variability in satellite ocean color and its potential applications to algorithm development. *Remote Sensing of Environment*, *112*, 4186–4203.

Cannizzaro, J. P., Hu, C., Carder, K. L., Kelble, C. R., Melo, N., Johns, E. M., Vargo, G. A., & Heil, C. A. (in press). On the accuracy of SeaWiFS ocean color data products on the West Florida Shelf. Journal of Coastal Research. http://dx.doi.org/10.2112/JCOASTRES-D-12-00223.1.

Chang, G. C., Dickey, T. D., Mobley, C. D., Boss, E., & Pegau, W. S. (2003). Toward closure of upwelling radiance in coastal waters. *Applied Optics*, *42*, 1574–1582.

Clark, D. K., Gordon, H. R., Voss, K. J., Ge, Y., Broenkow, W., & Trees, C. (1997). Validation of atmospheric correction over the oceans. *Journal of Geophysical Research*, *102*, 17209–17217.

Cropp, R. A., Gabric, A. J., McTainsh, G. H., Braddock, R. D., & Tindale, N. (2005). Coupling between ocean biota and atmospheric aerosols: Dust, dimethylsulphide, or artifact? *Global Biogeochemical Cycles*, *19*, GB4002.

Dierssen, H. M. (2010). Perspectives on empirical approaches for ocean color remote sensing of chlorophyll in a changing climate. *Proceedings of the National Academy of Sciences*, *107*, 17073–17078.

Eplee, R. E., Robinson, W. D., Bailey, S. W., Clark, D. K., Werdell, P. J., Wang, M., et al. (2001). Calibration of SeaWiFS. II. Vicarious techniques. *Applied Optics*, *40*, 6701–6718.

Fargion, G. S., Franz, B. A., Kwiatkowska, E. J., Pietras, C. M., Bailey, S. W., Gales, J., et al. (2004). SIMBIOS program in support of ocean color missions: 1997–2003. In R. J. Frouin, G. D. Gilbert, & D. Pan (Eds.), *Ocean remote sensing and imaging: II. Proceedings SPIE, Vol. 5155*. (pp. 49–60). : The Society of Photo-Optical Instrumentation Engineers.

Fishman, J., Iraci, L. T., Al-Saadi, J., Chance, K., Chavez, F., Chin, M., et al. (2012). The United States' next generation of atmospheric composition and coastal ecosystem

measurements: NASA's Geostationary Coastal and Air Pollution Events (GEO-CAPE) Mission. *Bulletin of the American Meteorological Society*, *2012, October*, 1547–1566. http://dx.doi.org/10.1175/BAMS-D-11-00201.1.

Franz, B. A., Bailey, S. W., Werdell, P. J., & McClain, C. R. (2007). Sensor-independent approach to the vicarious calibration of satellite ocean color radiometry. *Applied Optics*, *46*, 5068–5082.

Frouin, R., Schwindling, M., & Deschamps, P. -Y. (1996). Spectral reflectance of sea foam in the visible and near-infrared: In situ measurements and remote sensing implications. *Journal of Geophysical Research*, *101*, 14361–14371.

Gordon, H. R. (1997). Atmospheric correction of ocean color imagery in the Earth Observing System era. *Journal of Geophysical Research*, *102*, 17081–17106.

Gordon, H. R. (1998). In-orbit calibration strategy for ocean color sensors. *Remote Sensing of Environment*, *63*, 265–278.

Gordon, H. R., & Clark, D. K. (1981). Clear water radiances for atmospheric correction of coastal zone color scanner imagery. *Applied Optics*, *20*, 4175–4180.

Gordon, H. R., & Wang, M. (1994a). Influence of oceanic whitecaps on atmospheric correction of ocean-color sensors. *Applied Optics*, *33*, 7754–7763.

Gordon, H. R., & Wang, M. (1994b). Retrieval of water-leaving radiance and aerosol optical thickness over the oceans with SeaWiFS: A preliminary algorithm. *Applied Optics*, *33*, 443–452.

Gregg, W. W., & Casey, N. W. (2004). Global and regional evaluation of the SeaWiFS chlorophyll data set. *Remote Sensing of Environment*, *93*, 463–479.

Gregg, W. W., & Casey, N. W. (2010). Improving the consistency of ocean color data: A step toward climate data records. *Geophysical Research Letters*, *37*, L04605.

Harmel, T., Gilerson, A., Hlaing, S., Weidemann, A., Arnone, R., & Ahmed, S. (2012). Long Island Sound Coastal Observatory: Assessment of above-water radiometric measurement uncertainties using collocated multi and hyper-spectral systems: Reply to comment. *Applied Optics*, *51*, 3893–3899.

Hoge, F. E., & Lyon, P. E. (1996). Satellite retrieval of inherent optical properties by linear matrix inversion of oceanic radiance models: An analysis of model and radiance measurement errors. *Journal of Geophysical Research*, *101*, 16631–16648.

Hooker, S. B., Esaias, W. E., Feldman, G. C., Gregg, W. W., & McClain, C. R. (1992). *An overview of SeaWiFS and ocean color. NASA Tech. Memo., Vol. 104566*, Greenbelt, MD: National Aeronautics and Space Administration, Goddard Space Flight Center.

Hooker, S. B., & Maritorena, S. (2000). An evaluation of oceanographic radiometers and deployment methodologies. *Journal of Atmospheric and Oceanic Technology*, *17*, 811–830.

Hooker, S. B., & McClain, C. R. (2000). The calibration and validation of SeaWiFS data. *Progress In Oceanography*, *45*, 427–465.

Hooker, S. B., McClain, C. R., Firestone, J. K., Westphal, T. L., Yeh, E. -N., & Ge, Y. (1994). *The SeaWiFS bio-optical archive and storage system (SeaBASS): Part 1. NASA Tech. Memo., Vol. 104566*, Greenbelt, MD: National Aeronautics and Space Administration, Goddard Space Flight Center.

Hu, C., Carder, K. L., & Muller-Karger, F. E. (2001). How precise are SeaWiFS ocean color estimates? Implications of digitization-noise errors. *Remote Sensing of Environment*, *76*, 239–249.

Hu, C., Feng, L., Lee, Z., Davis, C. O., Mannino, A., McClain, C. R., et al. (2012a). Dynamic range and sensitivity requirements of satellite ocean color sensors: Learning from the past. *Applied Optics*, *51*, 6045–6062.

Hu, C., Lee, Z., & Franz, B. (2012b). Chlorophyll a algorithms for oligotrophic oceans: A novel approach based on three-band reflectance difference. *Journal of Geophysical Research*, *117*, C01011. http://dx.doi.org/10.1029/2011JC007395.

Huot, Y., Morel, A., Twardowski, M. S., Stramski, D., & Reynolds, R. A. (2008). Particle optical backscattering along a chlorophyll gradient in the upper layer of the eastern South Pacific Ocean. *Biogeosciences*, *5*, 495–507.

Lee, Z., Arnone, R., Hu, C., Werdell, P. J., & Lubac, B. (2010). Uncertainties of optical parameters and their propagations in an analytical ocean color inversion algorithm. *Applied Optics*, *49*, 369–381.

Lee, Z., Carder, K. L., & Arnone, R. A. (2002). Deriving inherent optical properties from water color: A multiband quasi-analytical algorithm for optically deep waters. *Applied Optics*, *41*, 5755–5772.

Lee, Z., Carder, K. L., & Du, K. (2004). Effects of molecular and particle scatterings on the model parameter for remote-sensing reflectance. *Applied Optics*, *43*, 4957–4964.

Lee, Z., & Hu, C. (2006). Global distribution of case-1 waters: An analysis from SeaWiFS measurements. *Remote Sensing of Environment*, *101*, 270–276.

Maritorena, S., d'Andon, O. H. F., Mangin, A., & Siegel, D. A. (2010). Merged satellite ocean color data products using a bio-optical model: Characteristics, benefits and issues. *Remote Sensing of Environment*, *114*, 1791–1804.

Mélin, F., Zibordi, G., & Berthon, J. -F. (2007). Assessment of satellite ocean color products at a coastal site. *Remote Sensing of Environment*, *110*, 192–215.

Moore, T. S., Campbell, J. W., & Dowell, M. D. (2009). A class-based approach to characterizing and mapping the uncertainty of the MODIS ocean chlorophyll product. *Remote Sensing of Environment*, *113*, 2424–2430.

Morel, A., Gentili, B., Claustre, H., Babin, M., Bricaud, A., Ras, J., et al. (2007). Optical properties of the "Clearest" natural waters. *Limnology and Oceanography*, *52*, 217–229.

Morel, A., & Maritorena, S. (2001). Bio-optical properties of oceanic waters: A reappraisal. *Journal of Geophysical Research*, *106*, 7163–7180.

National Aeronautics and Space Administration (2010). *Responding to the Challenge of Climate and Environmental Change: NASA's Plan for a Climate-Centric Architecture for Earth Observations and Applications from Space.* (48 pp. (http://science.nasa.gov/earth-science/))

National Research Council (2007). *Earth science and applications from space: National imperatives for the next decade and beyond*. Committee on earth science and applications from space: A community assessment and strategy for the future. National Research Council0-309-66714-3 (456 pp. (http://www.nap.edu/catalog/11820.html))

O'Reilly, J. E., Maritorena, S., Siegel, D. A., O'Brien, M. C., Toole, D., Mitchell, B. G., et al. (2010). Ocean color chlorophyll a algorithms for SeaWiFS, OC2, and OC4: Version 4. SeaWiFS postlaunch calibration and validation analyses, part 3. In S. B. Hooker, & E. R. Firestone (Eds.), *NASA Tech. Memo. 2000–206892*, *Vol. 11*, NASA Goddard Space Flight Center (49 pp.).

Park, Y. -J., & Ruddick, K. (2005). Model of remote-sensing reflectance including bidirectional effects for case 1 and case 2 waters. *Applied Optics*, *44*, 1236–1249.

Siegel, D. A., Maritorena, S., Nelson, N. B., Hansell, D. A., & Lorenzi-Kayser, M. (2002). Global distribution and dynamics of colored dissolved and detrital organic materials. *Journal of Geophysical Research*, *107*(C12), 3228. http://dx.doi.org/10.1029/2001JC000965 (2002).

Stumpf, R. P., & Werdell, P. J. (2010). Adjustment of ocean color sensor calibration through multi-band statistics. *Optics Express*, *18*, 401–412.

Szeto, M., Werdell, P. J., Moore, T. S., & Campbell, J. W. (2011). Are the world's oceans optically different? *Journal of Geophysical Research*, *116*, C00H04.

Toole, D. A., Siegel, D. A., Menzies, D. W., Neumann, M. J., & Smith, R. C. (2000). Remote-sensing reflectance determinations in the coastal ocean environment: Impact of instrumental characteristics and environmental variability. *Applied Optics*, *39*, 456–469.

Wang, M., & Bailey, S. W. (2001). Correction of sun glint contamination on the SeaWiFS ocean and atmosphere products. *Applied Optics*, *40*, 4790–4798.

Wang, P., Boss, E. S., & Roesler, C. (2005). Uncertainties of inherent optical properties obtained from semianalytical inversions of ocean color. *Applied Optics*, *44*, 4074–4085.

Wang, M., & Gordon, H. R. (2002). Calibration of ocean color scanners: How much error is acceptable in the near infrared? *Remote Sensing of Environment*, *82*, 497–504.

Wang, M., Knobelspiesse, K. D., & McClain, C. R. (2005). Study of the Sea-Viewing Wide Field-of-View Sensor (SeaWiFS) aerosol optical property data over ocean in combination with the ocean color products. *Journal of Geophysical Research*, *110*, D10S06.

Wang, M., & Shi, W. (2007). The NIR-SWIR combined atmospheric correction approach for MODIS ocean color data processing. *Optics Express*, *15*, 15722–15733.

Werdell, P. J., & Bailey, S. W. (2005). An improved in-situ bio-optical data set for ocean color algorithm development and satellite data product validation. *Remote Sensing of Environment*, *98*, 122–140.

Werdell, P. J., Bailey, S., Fargion, G., Pietras, C., Knobelspiesse, K., Feldman, G., et al. (2003). Unique data repository facilitates ocean color satellite validation. *EOS. Transactions of the American Geophysical Union*, *84*.

Werdell, P. J., Bailey, S. W., Franz, B. A., Morel, A., & McClain, C. R. (2007). On-orbit vicarious calibration of ocean color sensors using an ocean surface reflectance model. *Applied Optics*, *46*, 5649–5666.

Zaneveld, J. R., Barnard, A., & Boss, E. (2005). Theoretical derivation of the depth average of remotely sensed optical parameters. *Optics Express*, *13*, 9052–9061.

Zibordi, G., Berthon, J. -F., Mélin, F., D'Alimonte, D., & Kaitala, S. (2009). Validation of satellite ocean color primary products at optically complex coastal sites: Northern Adriatic Sea, Northern Baltic Proper and Gulf of Finland. *Remote Sensing of Environment*, *113*, 2574–2591.

Zibordi, G., Hooker, S. B., Berthon, J. F., & D'Alimonte, D. (2002). Autonomous above-water radiance measurements from an offshore platform: A field assessment experiment. *Journal of Atmospheric and Oceanic Technology*, *19*, 808–819.

Zibordi, G., Mélin, F., & Berthon, J. F. (2006). Comparison of SeaWiFS, MODIS and MERIS radiometric products at a coastal site. *Geophysical Research Letters*, *33*, L06617.